

B Cells Regulate Macrophage Phenotype and Response to Chemotherapy in Squamous Carcinomas

Nesrine I. Affara,^{1,10} Brian Ruffell,^{1,5,8,10} Terry R. Medler,⁵ Andrew J. Gunderson,⁵ Magnus Johansson,¹ Sophia Bornstein,⁷ Emily Bergsland,^{2,4} Martin Steinhoff,³ Yijin Li,⁹ Qian Gong,⁹ Yan Ma,⁹ Jane F. Wiesen,^{1,5} Melissa H. Wong,^{5,6,8} Molly Kulesz-Martin,^{5,6,8} Bryan Irving,^{9,11} and Lisa M. Coussens^{1,4,5,8,*}

¹Department of Pathology

²Department of Medicine

³Department of Dermatology

⁴Helen Diller Family Comprehensive Cancer Center

University of California, San Francisco, San Francisco, CA 94143, USA

⁵Department of Cell and Developmental Biology

⁶Department of Dermatology

⁷Department of Radiation Medicine

⁸Knight Cancer Institute

Oregon Health and Science University, Portland, OR 97239, USA

⁹Genentech, South San Francisco, CA 94080, USA

¹⁰Co-first author

¹¹Present address: CytomX Therapeutics, South San Francisco, CA 94080, USA

*Correspondence: cousseni@ohsu.edu

<http://dx.doi.org/10.1016/j.ccr.2014.04.026>

SUMMARY

B cells foster squamous cell carcinoma (SCC) development through deposition of immunoglobulin-containing immune complexes in premalignant tissue and Fc γ receptor-dependent activation of myeloid cells. Because human SCCs of the vulva and head and neck exhibited hallmarks of B cell infiltration, we examined B cell-deficient mice and found reduced support for SCC growth. Although ineffective as a single agent, treatment of mice bearing preexisting SCCs with B cell-depleting α CD20 monoclonal antibodies improved response to platinum- and Taxol-based chemotherapy. Improved chemoresponsiveness was dependent on altered chemokine expression by macrophages that promoted tumor infiltration of activated CD8⁺ lymphocytes via CCR5-dependent mechanisms. These data reveal that B cells, and the downstream myeloid-based pathways they regulate, represent tractable targets for anticancer therapy in select tumors.

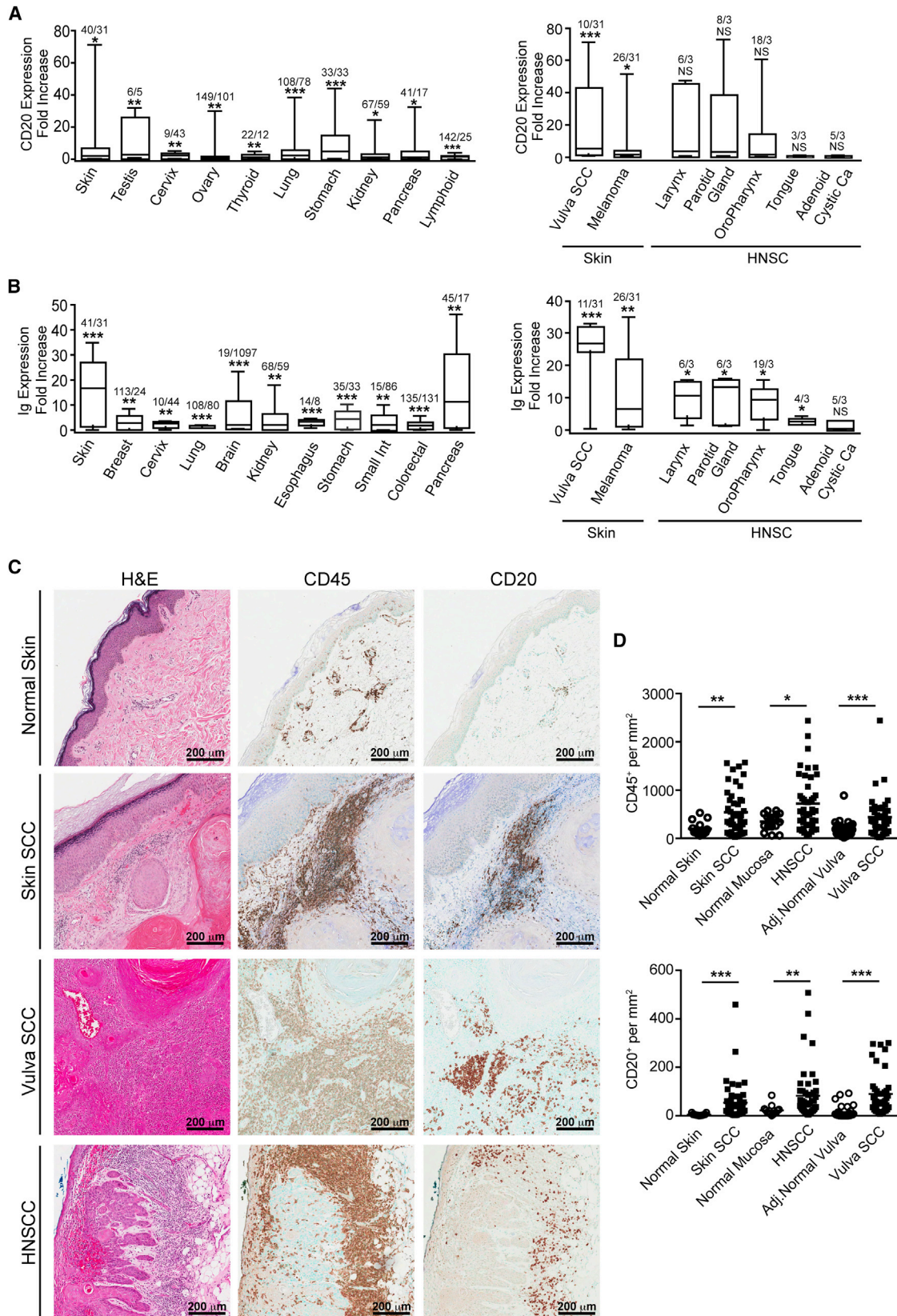
INTRODUCTION

As the central component of humoral immunity, B lymphocytes function in immunoglobulin (Ig) production, antigen presentation, and secretion of proinflammatory cytokines. Although critical for combating pathogens and aiding tissue healing, population-based studies have revealed increased systemic humoral immune responses, including increased deposition of Ig into tissues, in individuals afflicted with some chronic inflammatory

disorders associated with increased cancer risk. Cancer patients often develop antibodies to tumor-associated antigens; however, production of these antibodies does not necessarily confer protection, but instead often correlates with poor prognosis and decreased survival for several human cancer types. Population-based and experimental studies indicate that antitumor antibodies can facilitate tumor growth by promoting protumor immune responses and, in general, protecting malignant cells from cytotoxic T cell (CTL)-mediated killing (Gunderson and

Significance

The tumor immune microenvironment mediates all aspects of carcinogenesis, targeting of which is an attractive approach for enhancing traditional and targeted anticancer therapies. Herein, we identified human SCCs associated with high-risk human papillomaviruses (HPVs) as harboring immunoglobulin-producing B cells. Based on this, we evaluated a murine model of HPV16-regulated SCC for efficacy of B cell depletion as monotherapy, and in combination with standard-of-care chemotherapy. Administration of CD20 monoclonal antibodies significantly improved response to chemotherapy dependent on expression of an altered repertoire of chemokines expressed by macrophages, resulting in increased recruitment of cytotoxic T lymphocytes. These results indicate that the immune microenvironment in susceptible solid tumors can be reprogrammed to foster productive antitumor immune responses that bolster response to cytotoxic therapy.



(legend on next page)

Coussens, 2013; Tan and Coussens, 2007), thus supporting a role for B cells and humoral immunity in fostering cancer development. Support for a protumor role for B cells is further provided by the realization that growth of some subcutaneous solid tumors is retarded in syngeneic B cell-deficient mice, associated with enhanced local expression of T helper (Th) 1 cytokines and increased infiltration of tumors by CTLs (Qin et al., 1998; Shah et al., 2005; Tadmor et al., 2011).

Using a transgenic mouse model of de novo squamous cell carcinoma (SCC) development (Coussens et al., 1996), we reported that B cells and humoral immunity foster SCC development by activating Fc γ receptors (Fc γ Rs) on resident and recruited myeloid cells (Andreu et al., 2010; de Visser et al., 2005). Rather than infiltrating premalignant skin, Ig-secreting B cells exert distal effects on neoplastic tissue via production of circulating immune complexes (CICs) that accumulate in premalignant tissue (Andreu et al., 2010; de Visser et al., 2005). Following CIC engagement of activating-type I and activating-type III Fc γ Rs, tumor progression is fostered through activation of proangiogenic, tissue remodeling, and prosurvival pathways in resident and recruited myeloid cells, in particular, macrophages and mast cells (Andreu et al., 2010). Based on these data, we hypothesized that B cells, and the downstream myeloid-based pathways they regulate, represented tractable targets for combinatorial therapy in SCC. We therefore examined the preclinical efficacy of a B cell-depleting α CD20 monoclonal antibody (mAb) as an anticancer monotherapy, and in combination with chemotherapy (CTX).

RESULTS

B Cells in Human Solid Tumors

Unlike squamous carcinoma development in mice wherein premalignant and malignant tissues are poorly infiltrated by B cells (Andreu et al., 2010; de Visser et al., 2005; Schioppa et al., 2011), formation of tertiary/ectopic lymphoid structures containing B cells has been described for several human malignancies, including breast, cervical, ovarian, and non-small-cell lung cancer (Kobayashi et al., 2002; Nelson, 2010). Based upon these data, we hypothesized that ectopic production of either Ig or CD20 mRNA might signify human cancers wherein the humoral immune response fosters neoplastic progression or tumor growth, and thus identify carcinomas potentially amenable to B cell-targeted therapies.

To address this, we queried cDNA microarray data on a panel of human tumors from the BioExpress System and assessed CD20 (*MS4A1*) and Ig (*IGHG1*, *IGHG2*, *IGHV4-31*, *IGHM*) mRNA expression relative to corresponding normal tissue. Multiple tumor types displayed increased CD20 or Ig expression as

compared to nonmalignant tissue counterparts, but vulva SCCs and head and neck squamous cell carcinomas (HNSCCs) exhibited the greatest increase in CD20 and Ig mRNA expression, respectively (Figures 1A and 1B and Figure S1A available online), consistent with increased presence of CD20⁺ B cells in skin, vulva, and HNSCC as revealed by immunodetection (Figures 1C and 1D). Several Ig and FcR mRNAs were also found to be differentially expressed in HNSCC tumors relative to normal mucosa based on evaluation of a previously published data set (Ginos et al., 2004) using Oncomine (Rhodes et al., 2004) (Figure S1B). Notably, etiology for both vulva and HNSCCs is in part linked to human papillomavirus (HPV), with increasing incidence of carcinomas in both reflecting higher rates of HPV infection (Chaturvedi, 2010; Chaturvedi et al., 2011).

We have previously established that progression to carcinoma in a murine model of HPV16-induced SCC development (i.e., human keratin 14 [K14]-HPV16 mice) is dependent on binding of Igs to activating Fc γ Rs on infiltrating myeloid cells (Andreu et al., 2010). Importantly, K14-HPV16 mice are not tolerant to HPV oncoproteins (Andreu et al., 2010; Daniel et al., 2005), reflecting a similar scenario in HPV-positive oropharyngeal cancer wherein HPV-specific peripheral blood CD8⁺ T cells have been described previously (Albers et al., 2005; Wansom et al., 2010). We therefore sought to evaluate the therapeutic efficacy of B cell depletion (i.e., α CD20 mAbs) or inhibition of Fc γ signaling via a selective spleen tyrosine kinase (Syk) inhibitor (i.e., fostamatinib/R788) (Braselmann et al., 2006; Colonna et al., 2010) in either slowing or blocking progression of premalignant hyperplasia to dysplasia/carcinoma in situ.

Prevention of Premalignant Dysplasia by B Cell Depletion or Syk Kinase Inhibition

B cells, including mature B cells and plasma cells, accumulate in lymphoid organs of K14-HPV16 mice when neoplastic skin is at an early premalignant stage (Figures S2A–S2G). Accordingly, we conducted a prevention trial treating K14-HPV16 mice, starting at 1 month of age, with α CD20 mAbs to effectively deplete B cells, as well as with the potent Syk inhibitor fostamatinib/R788, starting at 1 month of age, when neoplastic skin exhibited a low-grade hyperplastic state throughout, and continuing to 4 months of age when neoplastic skin instead contained focal areas of low/high-grade dysplasia (Figure 2A). R788 is an orally bioavailable small molecule with potent Syk kinase inhibitory activity, whose active metabolite (R406) binds the ATP binding pocket of Syk and inhibits its kinase activity as an ATP-competitive inhibitor (inhibitor constant [K_i] = 30 nM) (Bahjat et al., 2008; Braselmann et al., 2006). Syk plays a key role in signaling

Figure 1. CD20 and Ig mRNA Expression in Human Cancers

(A and B) Relative CD20 (A) and Ig (B) mRNA expression in a panel of human cancers. Data are represented as box-and-whisker plots depicting median fold change value compared to normal tissue, displaying the first and third quartiles at the end of each box, with the maximum and minimum at the ends of the whiskers. Number of human cancer tissue/number of normal tissue is shown for each organ. Shown are tissues with statistically significant differences between cancer tissue and control normal tissue, with significance determined via Wilcoxon rank-sum test, with *p < 0.05, **p < 0.01, and ***p < 0.001.

(C) Representative histology of skin, vulva, and HNSCC in comparison to normal skin tissue. From left to right are hematoxylin and eosin staining (H&E) and immunohistochemistry (IHC) staining for CD45⁺ leukocytes and CD20⁺ B cells.

(D) Density of CD45⁺, CD20⁺, and CD8⁺ cells as determined by automated counting of IHC-stained sections. Ca, carcinoma.

See Figure S1 for complete analysis.

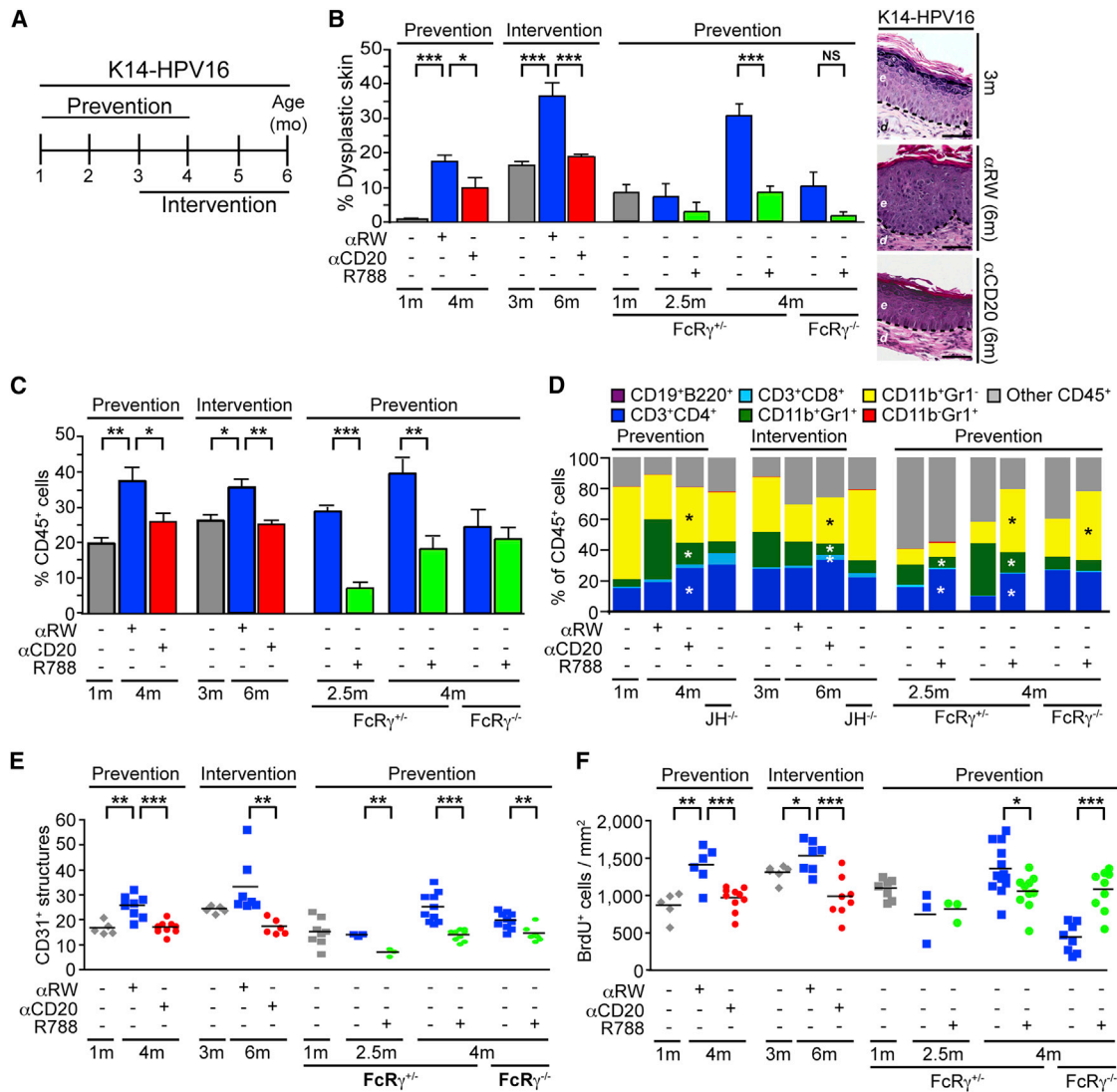


Figure 2. Inhibited Neoplastic Progression in K14-HPV16 Mice by Therapeutic α CD20 mAb or Fostamatinib

(A) Two stages of squamous carcinogenesis were evaluated: K14-HPV16 mice were enrolled at 1 month of age and received α CD20 or isotype control α RW at a 2-week interval until mice were 4 months of age (prevention), and B cell depletion or Syk inhibition was initiated at 3 months of age at a 2-week interval until mice were 6 months of age (intervention). Fostamatinib (R788), an orally bioavailable Syk kinase inhibitor, was administered through chow ad libitum at 2.0 g/kg/day to HPV16/ $FcR\gamma^{+/+}$ and HPV16/ $FcR\gamma^{-/-}$ mice at 1 month of age as compared to mice receiving control chow until 4 months of age.

(B) Percentages of ear skin (area) exhibiting dysplasia by 4 or 6 months of age following α CD20 mAb or fostamatinib administration. Values represent percentages of dysplastic lesions compared to whole ear skin per mouse with five to ten mice per experimental group. Results shown represent mean \pm SEM. Representative H&E sections from the α CD20 mAb intervention study are shown to the right. Scale bars, 50 μ m.

(C) Percentages of CD45⁺ immune cells in single-cell suspensions of skin as assessed by flow cytometry. Results shown represent mean \pm SEM.

(D) Immune cell lineage analysis by flow cytometry as percentages of total CD45⁺ leukocyte infiltrates in ear tissue.

(E) Angiogenic vasculature in skin of cohorts as evaluated by CD31/platelet endothelial cell adhesion molecule-1 IHC. Values represent average of five high-power fields of view per mouse.

(F) Keratinocyte proliferation in skin of mice cohorts as assessed by automated counting of BrdU-positive keratinocytes per square millimeter of premalignant tissue. Data reflect three or more mice per group; statistical significance was determined via an unpaired t test, with * p < 0.05, ** p < 0.01, and *** p < 0.001. See also Figure S2.

downstream of activating FcRs and B cell receptors (BCRs), and in several other cell lineages where activation leads to phosphorylation of Syk and signal transduction via activation of phospholipase $C\gamma$ and/or AKT. Notably, expression of mRNAs for both Syk and Bruton's tyrosine kinase (BTK), another key signaling molecule downstream of FcRs and BCRs, was increased in

HNSCC tumors relative to normal mucosa (Figure S1B). Phosphorylated BTK was also prominent in HNSCC tissue sections in CD20⁺ B cells and other stromal cells, as compared to normal mucosa (Figure 1C).

Administration of α CD20 mAbs to K14-HPV16 mice, but not a Ragweed-specific isotype control (α RW), effectively depleted B

cells in peripheral blood and secondary lymphoid organs (Figures S2H–S2L), including a partial depletion of CD19⁺CD1d^{hi}CD5⁺ B regulatory cells (Figure S2M), a subset of CD23^{lo}CD21^{hi} marginal zone B cells (Figure S4B) implicated in repressing antitumor immunity in two-stage skin carcinogenesis (Schioppa et al., 2011), and in suppressing lymphoma (Horikawa et al., 2011). Critically, α CD20 mAb treatment reduced levels of circulating IgG₁ (Figure S2N) and presence of autoantibodies against collagen I (Figure S2O); and consistent with a role of CIC deposition in skin of fostering neoplastic progression via Fc γ Rs, treatment with either α CD20 mAb or fostamatinib effectively blocked progression to dysplasia in the prevention trial (Figure 2B).

Because Ig deposition into neoplastic skin of K14-HPV16 mice becomes pronounced between 2 and 3 months of age, we also conducted an intervention trial where 3-month-old K14-HPV16 mice with high-grade hyperplasia/low-grade focal dysplasia were treated with α CD20 mAbs to 6 months of age, when neoplastic skin exhibited broadly dysplastic regions of focal high-grade dysplasia/carcinoma in situ (Figure 2A). In this setting as well, B cell depletion via α CD20 mAb as monotherapy blocked progression to dysplasia and significantly induced regression to a hyperplastic phenotype (Figure 2B).

Impaired progression to dysplasia in both trials was associated with significantly reduced infiltration of neoplastic skin by CD45⁺ leukocytes (Figure 2C), encompassing reduced recruitment of CD11b⁺Gr1⁺F4/80⁻CD11c⁻ immature myeloid cells, mast cells, and Gr1⁺ cells, with increased infiltration by CD11b⁺Gr1⁻F4/80⁺CD11c⁻ macrophages, and T cells (Figure 2D; Figures S2P–S2S), similar to results reported for K14-HPV16/B cell-deficient and K14-HPV16/FcR γ -deficient mice (Andreu et al., 2010). In addition to limiting mast cell infiltration, R406, the active metabolite of fostamatinib, significantly reduced release of interleukin-4 (IL-4), tumor necrosis factor α (TNF- α), IL-23, IL-9, and transforming growth factor β (TGF- β) from IgG-stimulated bone marrow-derived mast cells in ex vivo assays (Figure S2T).

Moreover, similar to results reported for K14-HPV16/B cell-deficient and K14-HPV16/FcR γ -deficient mice (Andreu et al., 2010), the reduced and altered infiltration by leukocytes in α CD20 mAb- and fostamatinib-treated K14-HPV16 mice was associated with decreased development of angiogenic vasculature (Figure 2E) that translated into diminished keratinocyte hyperproliferation (Figure 2F). Taken together, these data indicate that B cell depletion and Syk kinase inhibition may represent therapeutic opportunities for prevention and/or intervention in K14-HPV16-positive squamous neoplasms.

B Cell-Deficient Mice Fail to Support Orthotopic SCC Tumor Growth

Given the increased expression of Ig mRNA in human SCCs (Figure 1) and the efficacy of α CD20 mAb in restricting premalignant progression in K14-HPV16 transgenic mice (Figure 2), we next sought to evaluate the antitumor efficacy of B cell depletion as either monotherapy or in combination with CTX. For this, we used SCC cell lines derived from K14-HPV16 mice (Arbeit et al., 1996) harboring de novo grade I well-differentiated (WDSC1) or poorly differentiated SCCs (PDSC5 clone 6). Similar to our results in syngeneic FcR γ -deficient mice (Andreu et al.,

2010), orthotopic SCC growth was significantly reduced in syngeneic B cell-deficient (JH^{-/-}) mice (Figures 3A and 3B), characterized by increased presence of CD45⁺ leukocytes, decreased bromodeoxyuridine (BrdU)-positive keratinocytes, increased cleaved caspase-3-positive cells, and decreased tumor vascularization, along with increased presence of CD8⁺ T cells (Figure S3A).

Neoadjuvant α CD20 mAb as Monotherapy and in Combination with CTX

These findings provided a compelling rationale for assessing α CD20 mAb in a therapeutic setting. Thus, we evaluated α CD20 mAb for efficacy in blocking development of syngeneic SCCs, as compared to slowing or inducing regression of pre-existent syngeneic SCCs. Mice were administered α CD20 mAb either at the time of tumor cell implantation and again at 2-week intervals (day 0; every 14 days), or instead when orthotopic tumors reached \sim 50 mm³ (day 12), and then every 14 days (Figure 3C). Using this strategy, CD19⁺B220⁺CD138⁻ mature B cells were efficiently depleted from lymphoid organs (spleen and bone marrow) (Figure S3B), culminating in reduced presence of circulating IgG₁ (Figure S3C). Whereas administration of α CD20 mAb concurrent with SCC implantation significantly slowed tumor growth to end-stage (Figure 3C; Figure S3D), accompanied by reduced development of angiogenic vasculature (Figure S3E), tumor growth was not significantly slowed when α CD20 mAb therapy was initiated after tumors were apparent (Figure 3C; Figures S3D and S3E), despite a significantly increased percentage of CD8⁺ T cells infiltrating tumors (Figure 3D; Figure S3E).

Based on the increased presence of CD8⁺ T cells in orthotopic SCCs of α CD20 mAb-treated mice, we reasoned that efficacy might be enhanced by combination treatment with CTX. Indeed, treatment of mice bearing preexistent SCCs with α CD20 mAb in combination with cisplatin (CDPP) resulted in tumor regression in all animals (Figure S4A), as compared to CDPP alone, which was without effect. However, mice treated with α CD20/CDPP exhibited a 50% survival rate, likely due to cumulative impairment of liver and renal function (Figure S4B), a clinically relevant outcome as it mirrors CDPP-associated renal toxicity in cancer patients administered concomitant rituximab (α CD20 mAb). Due to its reduced nephrotoxicity, we instead evaluated carboplatin (CBDCA) as an alternative alkylating-type cytotoxic agent that also had no significant effect on tumor growth alone, but significantly slowed tumor growth when combined with α CD20 mAb throughout duration of the CTX cycle (Figure 4A), without evidence of toxicity or morbidity (Figure S4B), thus achieving a more favorable outcome.

To determine whether enhanced response to CTX was restricted to platinum-based agents, we next evaluated the microtubule polymer stabilizer paclitaxel (PTX) in combination with α CD20 mAb and similarly found significantly slowed SCC growth during the treatment cycle (Figure 4B), associated with decreased serum IgG₁ (Figure S4C). Histological evaluation of tumors from combinatorial-treated mice revealed reduced malignant keratinocyte proliferation that was paralleled by increased cell death (cleaved caspase-3 positivity; Figure 4C). We also note a reduction in vascular density (CD31⁺ vessels;

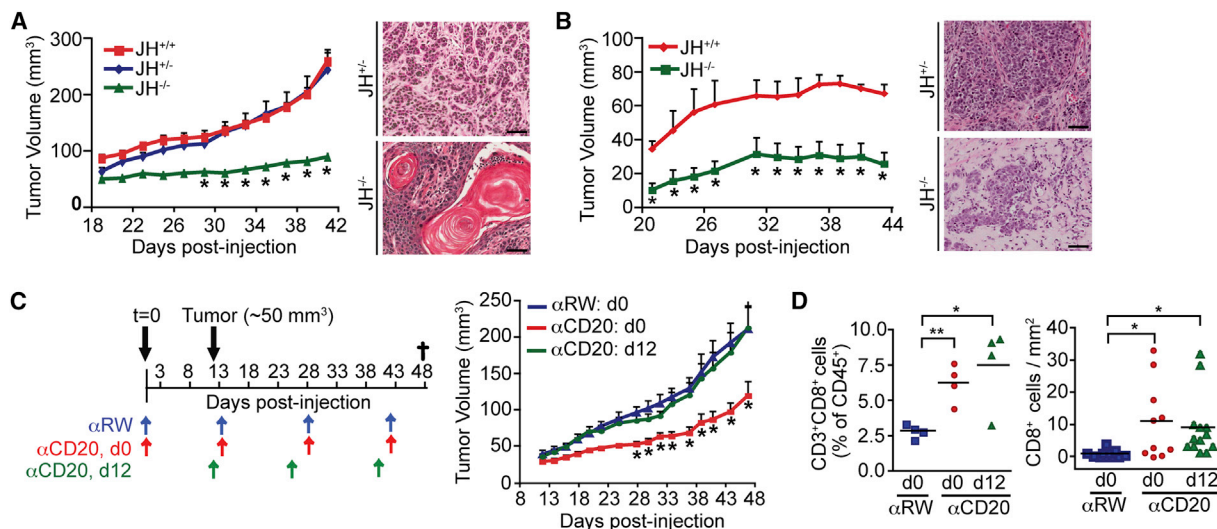


Figure 3. B Cell-Deficient Mice Limit SCC Tumor Growth

(A and B) Growth of (A) PDCS5 (clone 6; PDSC5.6) and (B) WDSC1 tumor cells injected orthotopically into syngeneic JH^{+/+} (red), JH^{+/-} (blue), and JH^{-/-} (green) mice. * denotes statistically significant differences in tumor growth between JH^{+/-} and JH^{-/-} mice. One of two representative experiments is shown and depicted as mean \pm SEM (≥ 10 mice per group). Representative H&E sections are shown to the right. Scale bars, 50 μ m.

(C) Growth of PDCS5.6-derived tumors in syngeneic mice treated with 2-week interval dosing of α CD20 (red) or α RW (blue) mAb either at the time of PDCS5.6 tumor cell inoculation (day 0), or alternatively in mice that received α CD20 mAb (green) following appearance of visible tumors (day 12). * indicates statistically significant differences between tumor growth in mice receiving α CD20 at day 12 compared to α CD20 or α RW at day 0. One of two representative experiments is shown depicted as mean \pm SEM (≥ 10 mice per group).

(D) Infiltration of CD8⁺ T lymphocytes within tumors from (C) as assessed by flow cytometry (left) and IHC (right). Unless otherwise indicated, statistical significance was determined via an unpaired t test, with * $p < 0.05$ and ** $p < 0.01$.

See also Figure S3.

Figure 4C; Figure S4D), although no apparent change in vascular leakage as measured by Evans blue assay (Figure S4D).

Given that α CD20 mAb improved responsiveness to PTX, we assessed the durability of tumor repression after one cycle of combined α CD20/PTX therapy and found that tumor regrowth was apparent within 10 days following cessation of PTX (Figure 4D). Because resistance to cytotoxic agents represents a major limitation of CTX, we evaluated a second cycle of α CD20/PTX therapy and found that tumors again responded to combined therapy, but again, that regrowth was evident following cessation of CTX (Figure 4D).

T Cell Infiltration in α CD20/PTX-Treated Tumors

To identify cellular mechanisms underlying slowing of tumor growth and increased efficacy of PTX in α CD20-treated mice, we evaluated leukocyte complexity of orthotopic SCCs by flow cytometry and found that SCCs responding to α CD20/PTX contained significantly increased infiltrates of both CD4⁺ and CD8⁺ T cells, as compared to tumors that regained growth kinetics following therapy cessation (Figure 4D). Increased CD8⁺ T cell infiltration in responding tumors from α CD20/PTX-treated mice was not unique to this experimental setting, as when we analyzed neoplastic skin from 4-month-old K14-HPV16/B cell-deficient, HK14-PV16/FcR γ -deficient, and K14-HPV16 mice enrolled in the intervention trial with α CD20 mAbs (Figure 1), we similarly observed increased presence of CD8⁺ T cells across all experimental groups as compared to controls (Figure 4E). To reveal the functional significance of increased T cell infiltrates,

CD4⁺ and CD8⁺ T cells were individually depleted from SCC-bearing α CD20/PTX-treated mice (Figure S5A), thus revealing that improved PTX responses in α CD20 mAb-treated mice were CD8⁺ T cell dependent (Figure 5A), but CD4⁺ T cell independent (Figure S5B). Moreover, depletion of CD8⁺ T cells reinstated the characteristic density of CD31⁺ vessels to growing tumors (Figure S5C).

To reveal molecular mediators regulating productive CD8⁺ T cell activity, we evaluated cytokine mRNA expression in SCCs of treated mice and found significantly increased levels of interferon α (*IFN α*) and granzyme B (*GzmB*), molecules involved in regulating CD8⁺ T cell activity (Figure 5B). In addition, this analysis revealed increased expression of the angiostatic molecules angiopoietin-1 (*Ang1*) and *CXCL10*, consistent with reduced development of vasculature in tumors from α CD20/PTX-treated mice (Figure 4C) and our previous results (Andreu et al., 2010).

Given these findings, we examined whether the improved PTX response was due to increased numbers of CD8⁺ T cells, or instead to improved functionality of infiltrating CD8⁺ T cells, by evaluating mRNA expression of SCC infiltrating CD8⁺ and CD4⁺ T cells isolated by fluorescence-activated cell sorting (FACS). Regardless of prior α CD20 treatment, T cells infiltrating SCCs had unchanged surface expression of activation markers CD69 and CD44 (Figure S5D), and they expressed similar levels of Th1/Th2/Th17-effector cytokines (*IL-2*, *IL-4*, *IL-5*, *IL-10*, *IL-13*, *IL-17a*, *IL-17f*, *IFN- γ* , *TNF- α*) and functional indicators of CD8⁺ T cell killing capability (e.g., *Gzma*, *Gzmb*, *Prf1*) (Figure S5E).

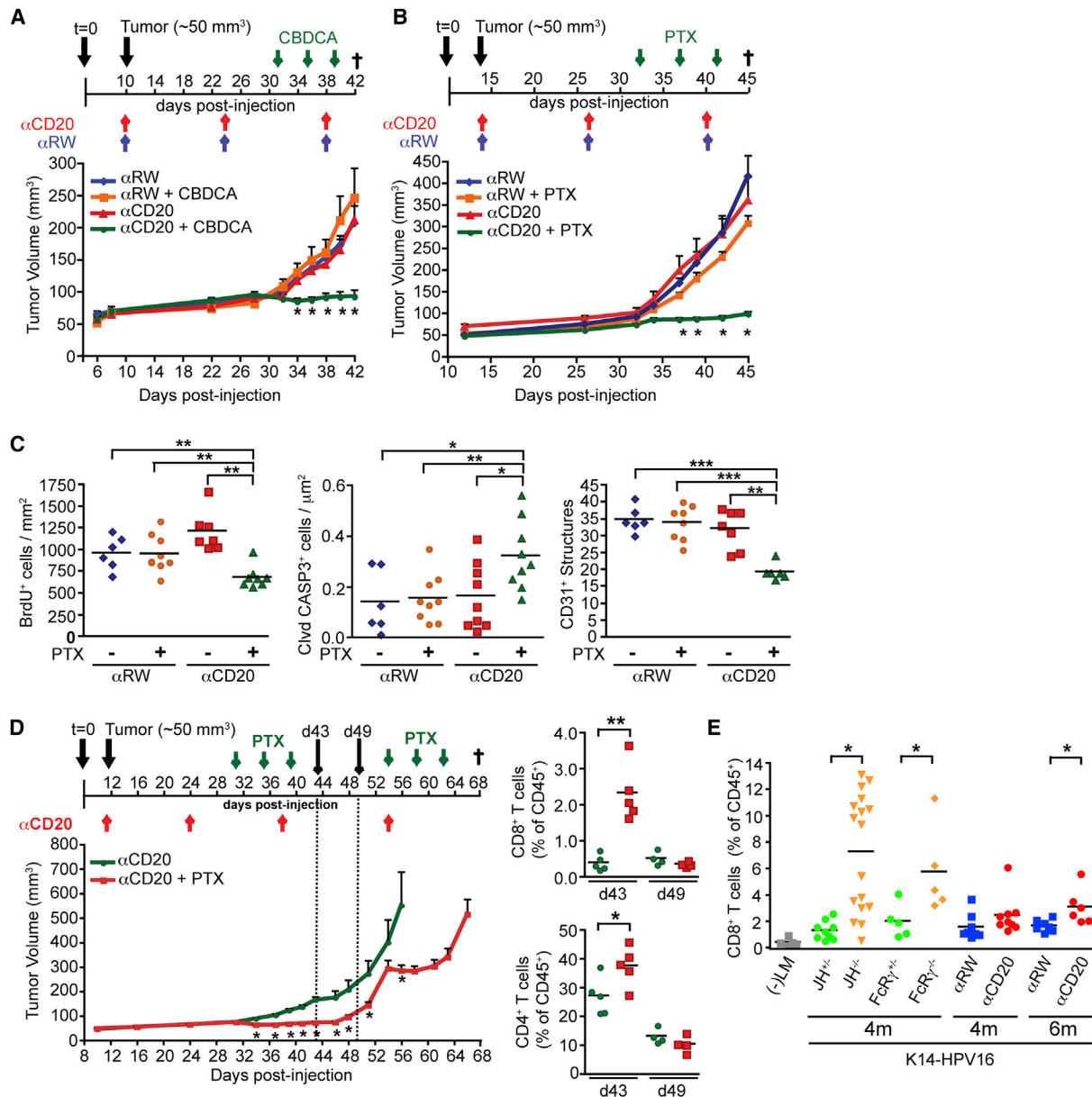


Figure 4. B Cell Depletion Sensitizes Established Tumors to Cytotoxic Agents

(A and B) Growth of PDSC5.6 SCCs in syngeneic mice receiving αCD20 or αRW mAbs at the time of visible tumor appearance (day 10), followed 3 weeks later by administration of the platinum-containing chemotherapeutic agents (A) CBDCA (50 mg/kg; every 4 days × three doses) (5–10 mice per group) or (B) PTX (12 mg/kg; every 4 days × three doses), with ten or more mice per group. One of at least two representative experiments is shown and depicted as mean ± SEM. * indicates statistically significant differences in tumor growth between αCD20 mAb/CTX, as compared to αCD20 mAb alone.

(C) Analysis of tissue sections from PDSC5.6 SCCs from (B): tumor cell proliferation, apoptosis, and vascular density by either automated quantitation of BrdU⁺, caspase-3⁺ cells, or manual counting of CD31⁺ structures in five high-power fields of view per mouse.

(D) Growth of PDSC5.6 SCCs in mice receiving multiple cycles of therapy (as shown) (≥ 17 mice per group). Results shown represent mean ± SEM. Presence of CD8⁺ and CD4⁺ T cells in PDSC5.6-derived SCCs, determined by flow cytometry, as percent of total CD45⁺ leukocytes within tumors at day 43 (stasis) and day 49 (regrowth) shown graphically on right.

(E) Infiltration of CD8⁺ T lymphocytes into premalignant skin from 4-month-old K14-HPV16/B cell-deficient mice, K14-HPV16/FcγR^{-/-} mice, and K14-HPV16 mice enrolled in the intervention trial with αCD20 mAbs as assessed by flow cytometry as a percentage of CD45⁺ cells (5–17 mice per group). Unless otherwise indicated, statistical significance was determined via an unpaired t test, with *p < 0.05, **p < 0.01, and ***p < 0.001.

See also Figure S4.

Although changes to a subset of cells would have been masked by our grouped analysis, these results suggested the improved therapeutic response associated with αCD20/PTX combined

therapy was due to reprogramming of the immune microenvironment to favor either survival or infiltration of CD8⁺ T cells that in turn enhanced tumor cell killing.

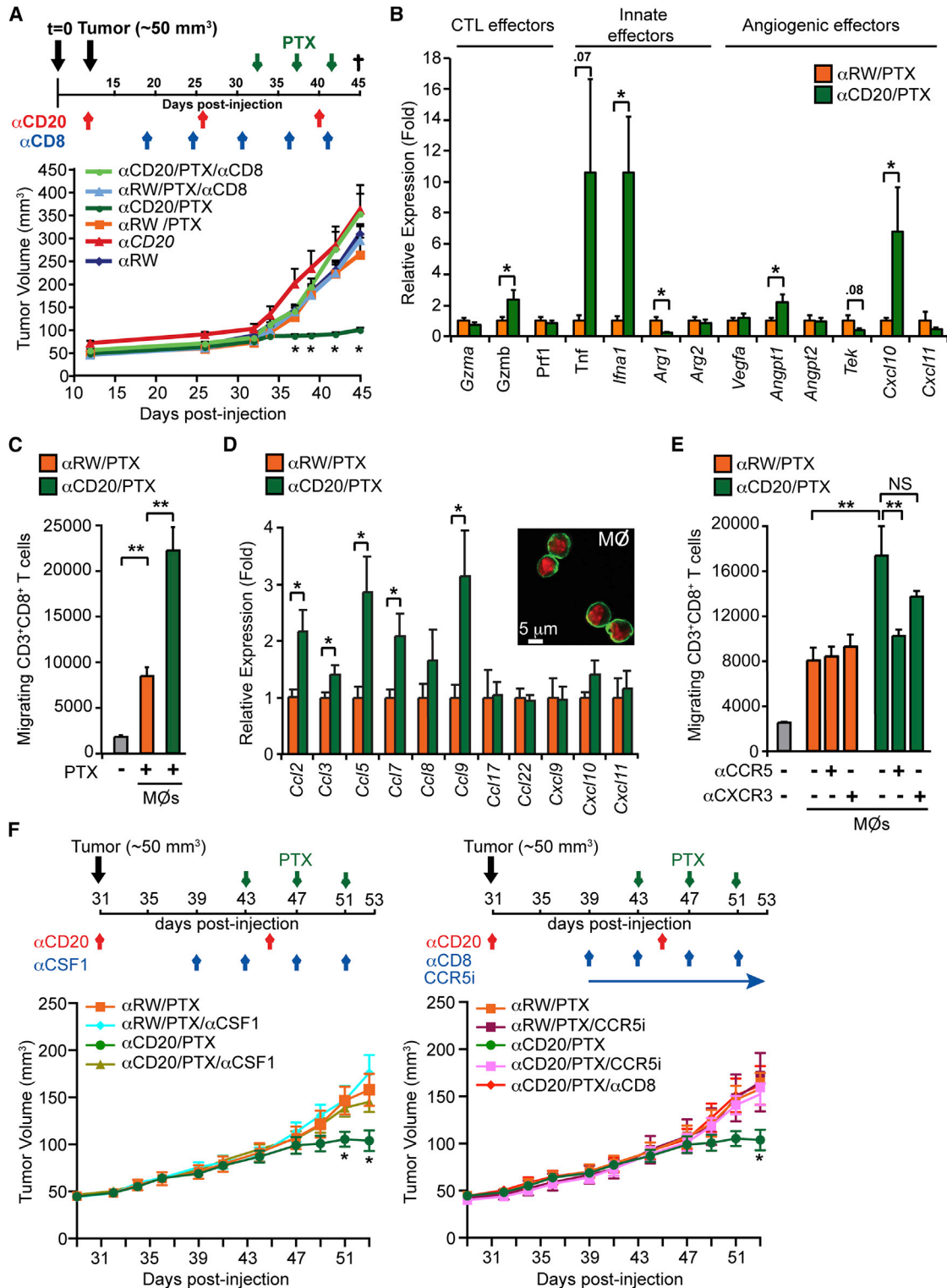


Figure 5. Combination αCD20 mAb Plus CTX Inhibits SCC Tumor Growth by CD8⁺ T Cell-Dependent Mechanisms

(A) Tumor growth of PDSC5.6-derived SCCs in mice treated with αCD20 mAb, or αCD8 (clone YTS169.4; 500 μg)-depleting mAb, alone or in combination with PTX, as depicted by treatment regimen. One of two representative experiments is shown and depicted as mean ± SEM. * indicates statistically significant differences in tumor growth between αCD20/PTX-treated mice compared to mice receiving αCD20 mAb alone (5–10 mice per group).

(B) mRNA expression of PDSC5.6 SCCs from PBS-perfused αCD20/PTX-treated mice compared to mice receiving αRW/PTX at day 45 of treatment regimen.

(legend continued on next page)

Macrophage Programming Regulates CD8⁺ T Cell Recruitment

Given our previous findings that macrophages are functionally reprogrammed to favor a more Th1-type (classically activated or “M1-type”) inflammatory state in K14-HPV16 mice lacking either B cells or Fc γ Rs (Andreu et al., 2010), we postulated that α CD20 mAb therapy was similarly reprogramming macrophages in SCCs of treated mice and that a macrophage-dependent mechanism differentially regulated CD8⁺ T cell infiltration. To investigate this hypothesis, we purified splenic CD8⁺ T cells (Figure S5F) and evaluated their chemotactic response to conditioned medium derived from FACS-sorted CD11b⁺ Ly6C⁻ Ly6G⁻ F4/80⁺ MHCII⁺ macrophages isolated from SCCs of α CD20/PTX versus α RW/PTX-treated mice (Figure S5G) and revealed a significant increase in CD8⁺ T cell recruitment in response to conditioned medium from α CD20/PTX-derived macrophages (Figure 5C). mRNA expression analysis of CD11b⁺ Gr1⁻ CD11c⁻ F4/80⁺ MHCII⁺ macrophages isolated from SCCs of α CD20/PTX-treated versus control mice revealed increased mRNA expression of several chemokines variably implicated in leukocyte recruitment, including *Ccl2*, *Ccl3*, *Ccl5*, *Ccl7*, and *Ccl9* (Figure 5D), but no significant changes in other genes associated with macrophage repolarization, including *Il1b*, *Il6*, *Il10*, *Il12a*, *Cd163*, *Msr1*, *Arg1*, or *Ym1* (data not shown). Splenic CD8⁺ T cells expressed CCR5 (binds CCL3, CCL4, and CCL5) and CXCR3 (binds CXCL10, CXCL11, and CXCL12) (Figure S5H), both of which have been linked to robust antitumor responses (González-Martín et al., 2011; Hong et al., 2011). Thus, we evaluated the effect of CCR5 and CXCR3 blockade on CD8⁺ T cell chemotaxis *ex vivo* and found that an α CCR5-blocking mAb alone abated CD8⁺ T cell chemotaxis to levels observed with macrophages isolated from SCCs of control α RW/PTX-treated mice (Figure 5E). Importantly, limiting *in vivo* tumor infiltration of macrophages with a neutralizing mAb to colony-stimulating factor 1 (α CSF1) (Figure S5I) blocked the combinatorial effect of α CD20/PTX treatment (Figure 5F) and restored the density of CD31⁺ vessels in SCCs to characteristic levels (Figure S5J). The combinatorial effect of α CD20/PTX treatment was similarly reversed by depletion of CD8⁺ T cells and also by use of the CCR5 inhibitor maraviroc (Figure 5F), collectively indicating that response to CTX in SCCs is regulated by CCR5-positive CD8⁺ T cells responding to macrophages programmed by humoral immunity (Figure 6). In support of a central role for CCL5/CCR5 in mediating a cytotoxic T cell response in SCC

patients, we found a significant correlation between expression of *CCL5* and expression of *PRF1*, *GZMA*, *GZMB*, and *CD69* (Figure S5K) in human HNSCC (Ginos et al., 2004).

DISCUSSION

Herein, we provide evidence that therapeutic strategies aimed at depleting B cells and/or dampening humoral immunity represent tractable targets for anticancer therapy in SCC. In preclinical prevention and intervention trials, treatment of K14-HPV16 transgenic mice with B cell-depleting α CD20 mAbs or a Syk inhibitor as monotherapy prevented neoplastic progression to the dysplastic/carcinoma *in situ* state. Although SCC growth was significantly slowed in either B cell- or Fc γ R-deficient mice (Andreu et al., 2010), treatment of syngeneic mice bearing preexistent orthotopic SCCs was without consequence following α CD20 mAb monotherapy. However, when α CD20 mAb was delivered in combination with CTX (CDPP, CBDCA, and PTX), SCC growth was significantly slowed, accompanied by reduced tumor vascular density and increased T cell infiltration, effects not achieved by administration of CTX alone. Improved SCC response to CTX in α CD20 mAb-treated mice was dependent on presence of “reprogrammed” macrophages producing CCR5 ligands, because depletion of either macrophages or CD8⁺ T cells restored SCC growth kinetics and vascular density to characteristic levels. Together, these data indicate that myeloid-based pathways regulated by humoral immunity limit SCC responses to CTX not only by fostering tumor angiogenesis, but also by impairing CD8⁺ T cell infiltration into tumors. Immune microenvironments in solid tumors can therefore be effectively reprogrammed to elicit productive antitumor immune responses that bolster response to cytotoxic therapy, provided that specific protumoral immune pathways can be identified and therapeutically targeted.

Treatment of solid tumors with CTX, although often useful for palliation or prolonging life in the setting of advanced disease, remains limited, with survival benefit often measured in months for some tumor types. Having an adjunctive therapeutic option to reverse or minimize chemoresistance, or to provide additive benefit through alternate mechanisms (immunomodulation), represents an attractive therapeutic strategy. Recent approval of ipilimumab, an anti-CTLA4 mAb for use in malignant melanoma (Hodi et al., 2010), and sipileucil-T, a dendritic cell vaccine that prolongs survival but not disease-free survival in

(C) *Ex vivo* recruitment of purified splenic CD8⁺ T lymphocytes in response to conditioned medium derived from FACS-sorted tumor-associated macrophages (CD11b⁺ Ly6C⁻ Ly6G⁻ F4/80⁺ MHCII⁺) isolated from PDSC5.6 SCCs of α CD20/PTX versus α RW/PTX-treated mice assessed using a Boyden chamber assay. Data are representative of two independent experiments.

(D) Cytokine mRNA expression of FACS-sorted macrophages (CD11b⁺ Ly6C⁻ Ly6G⁻ F4/80⁺ MHCII⁺) isolated from PDSC5.6-derived SCCs from α CD20/PTX versus α RW/PTX-treated mice at day 45 of treatment regimen. Inset shows representative confocal microscopy showing morphology of sorted macrophages visualized by β -actin (green) and DAPI (red) staining. Data represent mean fold change \pm SEM in expression compared to α RW/PTX treatment group (n = 8 per group).

(E) *Ex vivo* chemotaxis of purified splenic CD8⁺ T lymphocytes in response to conditioned medium derived from FACS-sorted macrophages (CD11b⁺ Ly6C⁻ Ly6G⁻ F4/80⁺ MHCII⁺) isolated from PDSC5.6 SCCs in α CD20/PTX- versus α RW/PTX-treated mice assessed in the presence or absence of blocking antibodies against CCR5 (10 μ g/ml) or CXCR3 (10 μ g/ml). Samples were assayed in triplicates for each tested condition with pooled samples from ten tumors. Data are displayed as mean \pm SEM. Statistical significance for (B)–(E) was determined via an unpaired t test, with *p < 0.05, **p < 0.01, and ***p < 0.001.

(F) Relative orthotopic growth of PDSC5.6 SCCs in syngeneic mice following administration of PTX in mice pretreated with α CD20 mAb, α CD8-depleting mAb (clone YTS169.4), α CSF1-neutralizing mAb (clone 5A1), or the CCR5 inhibitor maraviroc (CCR5i) as depicted by treatment regimen shown. Data represent mean \pm SEM. * indicates statistically significant differences in tumor growth between α CD20/PTX-treated mice as compared to all other groups as determined by two-way ANOVA (more than eight mice per group).

See also Figure S5.

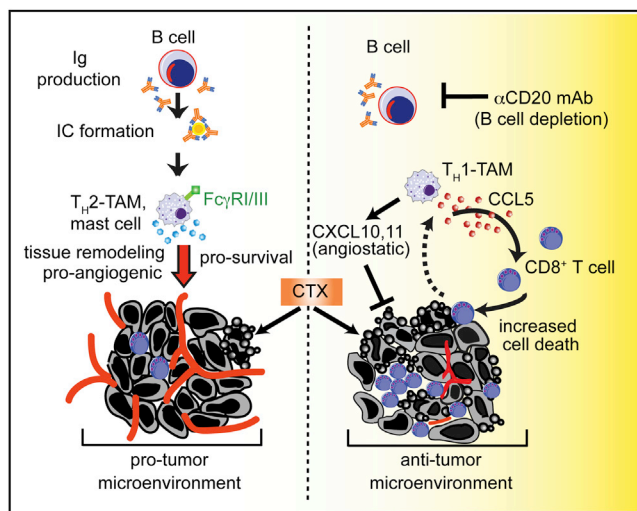


Figure 6. B Cell Depletion Repolarizes Tumor-Associated Macrophages in SCC

Cartoon showing a putative model for improved chemotherapeutic responses in SCCs following B cell depletion. Left: during tumor development, autoantibody production by B cells leads to deposition of immune complexes (IC) within neoplastic tissue. Signaling of these complexes through activating Fc γ R activates several protumor pathways, including angiogenic, tissue remodeling, and pro-survival pathways in mast cells and Th2-tumor-associated macrophages (TAMs). Right: α CD20 mAb therapy reduces presence of B cells and Ig, the absence of which fosters development of TAMs that instead express increased levels of angiostatic (CXCL10, 11), and CCR chemokines that enhance CD8 $^{+}$ T cell infiltration of malignant tumors culminating in improved response to CTX. Tumor growth to end-stage is thereby significantly slowed by enhanced cytotoxic effects on tumor cells and indirectly through effects on vasculature.

hormone-refractory prostate cancer (Kantoff et al., 2010; Small et al., 2006), engenders not only support for immunotherapy in general, but also the concept that immune responses to cancer can be redirected for therapeutic gain. Although neither ipilimumab nor sipileucil-T is currently approved for use in conjunction with CTX, it is intriguing to speculate that their efficacy would be improved if administered following CTX, or in combination with therapies that blunt protumor immunity while also favoring an antitumor immune microenvironment. Results presented herein reveal that these types of responses can indeed be generated by combining α CD20 mAb with CTX, similarly to that achieved by delivery of CSF1 antagonists with CTX in mammary carcinomas (DeNardo et al., 2011). Although both modalities slow tumor growth dependent on CD8 $^{+}$ T cells, these improvements are achieved by distinct molecular mechanisms resulting from lymphoid-based regulation of myeloid cell programming. These distinctions may reflect organ-specific mechanisms governing immune response, or nuances of the oncogenic drivers of solid tumor development.

Clinically, vulva and oropharyngeal malignancies are typically of a high-risk HPV viral etiology (Chaturvedi, 2010); thus, K14-HPV16 mice phenocopy neoplastic progression in these tissues and likely recapitulate a protumorigenic role for B cells and/or humoral immunity in these locales. This assertion is consistent with results from screening a diverse assortment of human solid

tumors for evidence of B cell infiltration, i.e., CD20 and/or Ig mRNA expression, wherein vulva and HNSCCs contained significantly increased levels of CD20 and Ig mRNA, consistent with histological evaluation of B cells in tumor tissue of these cancers as well as in human cutaneous SCCs. Several other human tumor types exhibited significant increases in CD20 and/or Ig mRNA as compared to corresponding *normal* tissue. B cell-deficient mice have previously been reported to also resist growth of a range of syngeneic tumors, including thymoma, colon, and mammary (Barbera-Guillem et al., 2000; Inoue et al., 2006; Shah et al., 2005; Tadmor et al., 2011), but in most instances these studies used nonorthotopic subcutaneous implantation. In several of these models, the protumorigenic role of B cells related to suppression of CD8 $^{+}$ T cell responses either directly through IL-10 (Inoue et al., 2006; Schioppa et al., 2011; Wong et al., 2010) or IL-15 (Chapoval et al., 1998), or indirectly through TGF- β and generation of regulatory T cells (Oikhanud et al., 2011; Tadmor et al., 2011). Whereas our previous findings indicated a role for Igs and CICs in mediating these effects (Andreu et al., 2010; de Visser et al., 2005), in other tumor models, adoptive transfer of B lymphocytes, but not serum, restored tumor growth accompanied by reduced Th1 cytokines and CTL responses, suggestive of antibody-independent mechanisms (Ammirante et al., 2010; Shah et al., 2005). Because B cells infiltrate human SCCs, unlike what has been observed in murine models of HPV16-induced SCCs (Andreu et al., 2010; de Visser et al., 2005) and chemical carcinogenesis-induced SCCs (Schioppa et al., 2011), we cannot rule out a potential role in human cancers for other B/plasma cell-derived factors such as granulocyte-macrophage-CSF (Rauch et al., 2012) or lymphotoxin (Moseman et al., 2012), as has been described for growth of subcutaneous androgen-independent metastatic prostate cancer cells (Ammirante et al., 2010).

B cell depletion as an adjunct to CTX in solid tumors should be relatively straightforward to address clinically. Rituximab is already an approved drug for B cell malignancies (McLaughlin et al., 1998), with no increased susceptibility to infection in patients with adult acute lymphoblastic leukemia, rheumatoid arthritis, or non-Hodgkin's lymphoma (Silverman, 2006). This is likely due to the fact that plasma cells are not depleted by α CD20 mAb therapy. We observed "normalized" IgG levels in tumor-bearing mice following α CD20 mAb therapy; thus, targeting pathological production of IgG through depletion of short-lived autoreactive cells without affecting immunity derived from plasma cells could be achieved in solid tumors, similar to that described for arthritis (Huang et al., 2010) and peripheral nervous system autoimmunity (Maurer et al., 2012). Although rituximab has few cumulative side effects and has been combined safely with many CTXs (Göckbuget and Hoelzer, 2006), it should be noted that rituximab has been reported to increase risk of some solid tumors in patients with lymphoma also treated with high-dose CTX and stem cell autografts (Tarella et al., 2011). Alternatively, the clinical success of ibrutinib, an irreversible small-molecule inhibitor of BTK (expressed by both B cells and myeloid cell subsets), engenders support for the notion that targeting protumoral B cells and humoral immune-activated pathways may improve overall survival in patients with tumors regulated by these pathways, when administered in combination with standard-of-care CTX.

Although studies presented herein identify SCCs as potentially benefiting from α CD20 mAb/CTX, the clinical relevance of α CD20 mAb may not be limited to just these solid tumors. Growth of experimental lung adenocarcinoma is reduced in B cell-deficient mice, with an improved CTX response observed upon coadministration with IL-15, a Th1 cytokine with IL-2-like antitumor bioactivities (Chapoval et al., 1998). Moreover, in a mouse model of melanoma, B cell deficiency provided a therapeutic advantage to a melanoma vaccine where enhanced tumor protection in the absence of B cells was associated with increased magnitude and longevity of specific cellular immune responses provoked by vaccination (Perricone et al., 2004). We also observed a striking increase in Ig expression in human pancreatic ductal adenocarcinoma samples and are currently evaluating whether this signature translates into a functional role in murine pancreas cancer models. Notably, a limited clinical study of advanced colon cancer patients treated with rituximab resulted in reduced numbers of CD21-hyperpositive lymphocytes associated with apparent 50% reduction in tumor burden with no ill effects due to therapy (Barbera-Guillem et al., 2000). Because human SCCs appear to be enriched with tumor promoting B cells, we propose these as tractable cancers in which to examine efficacy of α CD20 mAb, or other antagonists blocking protumoral B cell/humoral immunity programs, such as Syk or BTK inhibitors, in combination with CTX.

EXPERIMENTAL PROCEDURES

Microarray Data Normalization and Integration

Microarray data reflecting CD20 and Ig mRNA in human tumor samples were queried from a commercially available data set (BioExpress System, Gene Logic) originally generated on the Human Genome U133 Plus 2.0 Array (Affymetrix) and normalized by standard robust multichip average procedure. A single probe set of the highest variance among samples was chosen to represent CD20 (228592_at; *MS4A1*) and Ig (211430_s_at; *IGHG1*, *IGHG2*, *IGHV4-31*, *IGHM*), respectively. To ensure data consistency, results from additional probe sets were compared to a single probe set. Median value was used to calculate fold change of expression in tumor tissue compared to normal tissue. Statistical analyses were performed using Wilcoxon rank-sum test to compare mRNA expression levels to their corresponding normal tissue controls.

Immunohistochemistry

Staining on human tissue sections was performed as described previously (Ruffell et al., 2012). De-identified human tissue was received from the University of California, San Francisco (UCSF) Department of Pathology under approval from the UCSF Committee on Human Research (05028310), and the Oregon Health and Science University (OHSU) Department of Dermatology Molecular Profiling Resource (institutional review board [IRB] #809), with patient consent forms obtained at the time of tissue acquisition. The use of samples occurred under "exempt category 4" for individuals receiving de-identified biological specimens.

Animal Husbandry and In Vivo Studies

Generation and characterization of K14-HPV16 and JH^{-/-} mice have been described previously (Andreu et al., 2010). Briefly, K14-HPV16 transgenic mice represent a well-characterized model of multistage epithelial carcinogenesis where HPV16 early region genes are expressed under control of a K14 promoter, i.e., K14-HPV16 mice (Arbeit et al., 1994; Coussens et al., 1996, 1999, 2000; Daniel et al., 2003; de Visser et al., 2004, 2005; Rhee et al., 2004; van Kempen et al., 2002). By 1 month of age, K14-HPV16 mice develop hyperproliferative lesions (hyperplasias) throughout skin. Between 3 and 6 months of age, these hyperplasias progress into 100% penetrant focal dysplasias and are predisposed to progress into multiple histologic grades of SCC in ~50% of mice on the FVB/n strain background, 30% of which metastasize to

regional lymph nodes. Angiogenic vasculature is first evident in hyperplasias, development of which is linked to infiltration of innate immune cells (de Visser et al., 2004, 2005; van Kempen et al., 2002). All experiments with mice complied with National Institutes of Health guidelines and were approved by the UCSF Institutional Animal Care and Use Committee.

α CD20 mAb (clone 5D2, provided by Genentech) was generated by immunizing CD20-deficient mice with a murine pre-B cell line (300.19) transfected with murine *CD20*. cDNAs encoding heavy and light chain were cloned from hybridomas and further used for transfection and antibody production in Chinese hamster ovary cells. Ragweed-specific mouse IgG2a (α RW mAb) was used as an isotype control. K14-HPV16 mice received α CD20 (200 μ g) or α RW (200 μ g) mAb intraperitoneally (i.p.) at 2-week intervals commencing at 1 or 3 months of age. Mice bearing syngeneic orthotopic tumors received α CD20 mAb (200 μ g) or α RW mAb (200 μ g) either at the time of tumor cell inoculation (day 0) or following appearance of palpable transplantable tumors (e.g., day 12) at 2-week intervals for a total of three treatments. K14-HPV16/*FcR γ ^{+/-}* (≥ 18 mice per cohort) and K14-HPV16/*FcR γ ^{-/-}* (≥ 10 mice per cohort) mice were fed chow containing orally soluble fostamatinib (R788) at 2.0 g of fostamatinib per kg of chow, as compared to control chow (AIN-76A) (Rigel Pharmaceuticals) ad libitum beginning at 1 month of age and continuing for a total of 12 weeks. Formulated chow was prepared by Research Diets. R406 (R940406) is the active metabolite of fostamatinib that acts as an ATP-competitive inhibitor ($K_i = 30$ nM), thus selectively inhibiting Syk kinase activity as assessed using a large panel of Syk-dependent and -independent cell-based assays (Braselmann et al., 2006). Plasma R406 levels were monitored for 48, 51, 54, 57, and 58 hr, revealing peak plasma levels at 558 ng/ml in male FVB/n mice and peak levels in female FVB/n mice at 118.9 ng/ml (data not shown). Thus, using 2.0 mg/ml (10-fold higher than the tested dose), Syk kinase activity in female FVB/n mice was inhibited in vivo and was monitored as a function of plasma R406 levels and Syk kinase activity in peripheral blood leukocytes.

Orthotopic Tumor Transplantation

PDSC5 and WDSC cells (0.5×10^6 cells) were suspended in 100 μ l of basement membrane extract Matrigel (BD Pharmingen) in PBS (1:1) and inoculated orthotopically into back skin of 7-week-old female FVB/n mice. Transplantable tumors were measured at 2-day intervals using a digital caliper, and tumor volume was calculated using the equation V (mm³) = $a \times b^2/2$, where a is largest diameter and b is smallest diameter. To assess effects of PTX (12 mg/kg; Novaplus), CDPP (10 mg/kg; Hospira), and CBDCA (50 mg/kg; APP Pharmaceuticals) on tumor growth, tumor-bearing mice were pretreated with α CD20 mAb or α RW mAb as described above. Chemotherapeutic agents were injected intravenously at 4-day intervals 1 week following administration of the second dose of α CD20 or α RW mAb for a total of three treatments. Mice were sacrificed 4 days following the last chemotherapeutic dose. For tumor regression studies, mice were treated with α CD20 mAb/PTX following regrowth of transplantable tumors. Mice received PTX at a 4-day interval for a total of three treatments. For in vivo depletion studies, α CD4 (GK1.5) and α CD8 (YTS169.4) mAbs were administered i.p. at 500 μ g on day 4 following initial treatment with α CD20 mAb at a 5-day interval, whereas α CSF1 (5A1) antibodies (all from Bio X Cell) were administered i.p. at 1,000 μ g 4 days prior to the first chemotherapeutic dose, with subsequent doses of 500 μ g every 4 days. Clinical grade maraviroc was dissolved at 300 mg/l in drinking water for ad libitum dosing (Ochoa-Callejero et al., 2013).

Statistical Analyses

Statistical analyses were performed using Prism version 4 and/or InStat version 3.0a for Macintosh (both GraphPad). Specific tests included Mann-Whitney (unpaired, nonparametric, two-tailed), unpaired t test, and Wilcoxon rank-sum and are identified in the respective figures. p Values < 0.05 were considered statistically significant, with * p < 0.05, ** p < 0.01, and *** p < 0.001 unless otherwise indicated.

SUPPLEMENTAL INFORMATION

Supplemental Information includes Supplemental Experimental Procedures and five figures and can be found with this article online at <http://dx.doi.org/10.1016/j.ccr.2014.04.026>.

AUTHOR CONTRIBUTIONS

N.I.A. and B.R. contributed equally to this work through the design and execution of experiments, analysis of data, and preparation of the manuscript.

ACKNOWLEDGMENTS

We thank the Knight Cancer Center Flow Cytometry shared resource; Genentech for providing α CD20 and α RW mAbs; and members of the L.M.C. lab for critical discussion. We also thank the OHSU Department of Dermatology Molecular Profiling Resource (IRB #809) and the OHSU Knight Cancer Institute (NCI P30CA069533) for support of other Shared Core Resources used for studies herein. This work was supported by the American Association for Cancer Research and a NIH postdoctoral training grant in Molecular & Cellular Mechanisms in Cancer to N.I.A. (T32 CA108462); a Department of Defense Breast Cancer Research Program Fellowship to B.R. (W81XWH-09-1-0543); NIH/NCI training grants to T.R.M. (T32CA106195) and A.J.G. (T32AI078903-04); and grants from the NIH/NCI (R01 CA130980, R01 CA140943, R01 CA155331, U54 CA163123), a DOD BCRP Era of Hope Scholar Expansion Award (W81XWH-08-PRMRP-IIRA), the Susan B Komen Foundation (KG111084 and KG110560), and the Breast Cancer Research Foundation to L.M.C. Y.L., Q.G., Y.M., and B.I. are employees of Genentech. Work with fostamatinib disodium was performed under a sponsored research agreement with Rigel Pharmaceuticals, but no employees of Rigel had any involvement in data collection, analysis, or interpretation.

Received: December 8, 2013

Revised: February 13, 2014

Accepted: April 30, 2014

Published: June 5, 2014

REFERENCES

- Albers, A., Abe, K., Hunt, J., Wang, J., Lopez-Albaitero, A., Schaefer, C., Gooding, W., Whiteside, T.L., Ferrone, S., DeLeo, A., and Ferris, R.L. (2005). Antitumor activity of human papillomavirus type 16 E7-specific T cells against virally infected squamous cell carcinoma of the head and neck. *Cancer Res.* **65**, 11146–11155.
- Ammirante, M., Luo, J.L., Grivennikov, S., Nedospasov, S., and Karin, M. (2010). B-cell-derived lymphotoxin promotes castration-resistant prostate cancer. *Nature* **464**, 302–305.
- Andreu, P., Johansson, M., Affara, N.I., Pucci, F., Tan, T., Junankar, S., Korets, L., Lam, J., Tawfik, D., DeNardo, D.G., et al. (2010). FcR γ activation regulates inflammation-associated squamous carcinogenesis. *Cancer Cell* **17**, 121–134.
- Arbeit, J.M., Münger, K., Howley, P.M., and Hanahan, D. (1994). Progressive squamous epithelial neoplasia in K14-human papillomavirus type 16 transgenic mice. *J. Virol.* **68**, 4358–4368.
- Arbeit, J.M., Olson, D.C., and Hanahan, D. (1996). Upregulation of fibroblast growth factors and their receptors during multi-stage epidermal carcinogenesis in K14-HPV16 transgenic mice. *Oncogene* **13**, 1847–1857.
- Bahjat, F.R., Pine, P.R., Reitsma, A., Cassafer, G., Baluom, M., Grillo, S., Chang, B., Zhao, F.F., Payan, D.G., Grossbard, E.B., and Daikh, D.I. (2008). An orally bioavailable spleen tyrosine kinase inhibitor delays disease progression and prolongs survival in murine lupus. *Arthritis Rheum.* **58**, 1433–1444.
- Barbera-Guillem, E., Nelson, M.B., Barr, B., Nyhus, J.K., May, K.F., Jr., Feng, L., and Sampsel, J.W. (2000). B lymphocyte pathology in human colorectal cancer. Experimental and clinical therapeutic effects of partial B cell depletion. *Cancer Immunol. Immunother.* **48**, 541–549.
- Brasemann, S., Taylor, V., Zhao, H., Wang, S., Sylvain, C., Baluom, M., Qu, K., Herlaar, E., Lau, A., Young, C., et al. (2006). R406, an orally available spleen tyrosine kinase inhibitor blocks fc receptor signaling and reduces immune complex-mediated inflammation. *J. Pharmacol. Exp. Ther.* **319**, 998–1008.
- Chapoval, A.I., Fuller, J.A., Kremlev, S.G., Kamdar, S.J., and Evans, R. (1998). Combination chemotherapy and IL-15 administration induce permanent tumor regression in a mouse lung tumor model: NK and T cell-mediated effects antagonized by B cells. *J. Immunol.* **161**, 6977–6984.
- Chaturvedi, A.K. (2010). Beyond cervical cancer: burden of other HPV-related cancers among men and women. *J. Adolesc. Health* **46**, S20–26.
- Chaturvedi, A.K., Engels, E.A., Pfeiffer, R.M., Hernandez, B.Y., Xiao, W., Kim, E., Jiang, B., Goodman, M.T., Sibug-Saber, M., Cozen, W., et al. (2011). Human papillomavirus and rising oropharyngeal cancer incidence in the United States. *J. Clin. Oncol.* **29**, 4294–4301.
- Colonna, L., Catalano, G., Chew, C., D'Agati, V., Thomas, J.W., Wong, F.S., Schmitz, J., Masuda, E.S., Reizis, B., Tarakhovskiy, A., and Clynes, R. (2010). Therapeutic targeting of Syk in autoimmune diabetes. *J. Immunol.* **185**, 1532–1543.
- Coussens, L.M., Hanahan, D., and Arbeit, J.M. (1996). Genetic predisposition and parameters of malignant progression in K14-HPV16 transgenic mice. *Am. J. Pathol.* **149**, 1899–1917.
- Coussens, L.M., Raymond, W.W., Bergers, G., Laig-Webster, M., Behrendtsen, O., Werb, Z., Caughey, G.H., and Hanahan, D. (1999). Inflammatory mast cells up-regulate angiogenesis during squamous epithelial carcinogenesis. *Genes Dev.* **13**, 1382–1397.
- Coussens, L.M., Tinkle, C.L., Hanahan, D., and Werb, Z. (2000). MMP-9 supplied by bone marrow-derived cells contributes to skin carcinogenesis. *Cell* **103**, 481–490.
- Daniel, D., Meyer-Morse, N., Bergsland, E.K., Dehne, K., Coussens, L.M., and Hanahan, D. (2003). Immune enhancement of skin carcinogenesis by CD4+ T cells. *J. Exp. Med.* **197**, 1017–1028.
- Daniel, D., Chiu, C., Giraudo, E., Inoue, M., Mizzen, L.A., Chu, N.R., and Hanahan, D. (2005). CD4+ T cell-mediated antigen-specific immunotherapy in a mouse model of cervical cancer. *Cancer Res.* **65**, 2018–2025.
- de Visser, K.E., Korets, L.V., and Coussens, L.M. (2004). Early neoplastic progression is complement independent. *Neoplasia* **6**, 768–776.
- de Visser, K.E., Korets, L.V., and Coussens, L.M. (2005). De novo carcinogenesis promoted by chronic inflammation is B lymphocyte dependent. *Cancer Cell* **7**, 411–423.
- DeNardo, D.G., Brennan, D.J., Rexhepaj, E., Ruffell, B., Shiao, S.L., Madden, S.F., Gallagher, W.M., Wadhvani, N., Keil, S.D., Junaid, S.A., et al. (2011). Leukocyte complexity predicts breast cancer survival and functionally regulates response to chemotherapy. *Cancer Discov.* **1**, 54–67.
- Ginos, M.A., Page, G.P., Michalowicz, B.S., Patel, K.J., Volker, S.E., Pambuccian, S.E., Ondrey, F.G., Adams, G.L., and Gaffney, P.M. (2004). Identification of a gene expression signature associated with recurrent disease in squamous cell carcinoma of the head and neck. *Cancer Res.* **64**, 55–63.
- Gökbuget, N., and Hoelzer, D. (2006). Novel antibody-based therapy for acute lymphoblastic leukaemia. *Best Pract. Res. Clin. Haematol.* **19**, 701–713.
- González-Martín, A., Gómez, L., Lustgarten, J., Mira, E., and Mañes, S. (2011). Maximal T cell-mediated antitumor responses rely upon CCR5 expression in both CD4(+) and CD8(+) T cells. *Cancer Res.* **71**, 5455–5466.
- Gunderson, A.J., and Coussens, L.M. (2013). B cells and their mediators as targets for therapy in solid tumors. *Exp. Cell Res.* **319**, 1644–1649.
- Hodi, F.S., O'Day, S.J., McDermott, D.F., Weber, R.W., Sosman, J.A., Haanen, J.B., Gonzalez, R., Robert, C., Schadendorf, D., Hassel, J.C., et al. (2010). Improved survival with ipilimumab in patients with metastatic melanoma. *N. Engl. J. Med.* **363**, 711–723.
- Hong, M., Puaux, A.L., Huang, C., Loumagne, L., Tow, C., Mackay, C., Kato, M., Prévost-Blondel, A., Avril, M.F., Nardin, A., and Abastado, J.P. (2011). Chemotherapy induces intratumoral expression of chemokines in cutaneous melanoma, favoring T-cell infiltration and tumor control. *Cancer Res.* **71**, 6997–7009.
- Horikawa, M., Minard-Colin, V., Matsushita, T., and Tedder, T.F. (2011). Regulatory B cell production of IL-10 inhibits lymphoma depletion during CD20 immunotherapy in mice. *J. Clin. Invest.* **121**, 4268–4280.
- Huang, H., Benoist, C., and Mathis, D. (2010). Rituximab specifically depletes short-lived autoreactive plasma cells in a mouse model of inflammatory arthritis. *Proc. Natl. Acad. Sci. USA* **107**, 4658–4663.

- Inoue, S., Leitner, W.W., Golding, B., and Scott, D. (2006). Inhibitory effects of B cells on antitumor immunity. *Cancer Res.* 66, 7741–7747.
- Kantoff, P.W., Higano, C.S., Shore, N.D., Berger, E.R., Small, E.J., Penson, D.F., Redfern, C.H., Ferrari, A.C., Dreicer, R., Sims, R.B., et al.; IMPACT Study Investigators (2010). Sipuleucel-T immunotherapy for castration-resistant prostate cancer. *N. Engl. J. Med.* 363, 411–422.
- Kobayashi, A., Darragh, T., Herndier, B., Anastos, K., Minkoff, H., Cohen, M., Young, M., Levine, A., Grant, L.A., Hyun, W., et al. (2002). Lymphoid follicles are generated in high-grade cervical dysplasia and have differing characteristics depending on HIV status. *Am. J. Pathol.* 160, 151–164.
- Maurer, M.A., Rakocevic, G., Leung, C.S., Quast, I., Lukacisin, M., Goebels, N., Münz, C., Wardemann, H., Dalakas, M., and Lünemann, J.D. (2012). Rituximab induces sustained reduction of pathogenic B cells in patients with peripheral nervous system autoimmunity. *J. Clin. Invest.* 122, 1393–1402.
- McLaughlin, P., White, C.A., Grillo-Lopez, A.J., and Maloney, D.G. (1998). Clinical status and optimal use of rituximab for B-cell lymphomas. *Oncology* 12 (Huntingt), 1763–1769, discussion 1769–1770, 1775–1777.
- Moseman, E.A., Iannacone, M., Bosurgi, L., Tonti, E., Chevrier, N., Tumanov, A., Fu, Y.X., Hacohen, N., and von Andrian, U.H. (2012). B cell maintenance of subcapsular sinus macrophages protects against a fatal viral infection independent of adaptive immunity. *Immunity* 36, 415–426.
- Nelson, B.H. (2010). CD20+ B cells: the other tumor-infiltrating lymphocytes. *J. Immunol.* 185, 4977–4982.
- Ochoa-Callejero, L., Pérez-Martínez, L., Rubio-Mediavilla, S., Oteo, J.A., Martínez, A., and Blanco, J.R. (2013). Maraviroc, a CCR5 antagonist, prevents development of hepatocellular carcinoma in a mouse model. *PLoS ONE* 8, e53992.
- Olkhanud, P.B., Damdinsuren, B., Bodogai, M., Gress, R.E., Sen, R., Wejksza, K., Malchinkhuu, E., Wersto, R.P., and Biragyn, A. (2011). Tumor-evoked regulatory B cells promote breast cancer metastasis by converting resting CD4+ T cells to T-regulatory cells. *Cancer Res.* 71, 3505–3515.
- Perricone, M.A., Smith, K.A., Claussen, K.A., Plog, M.S., Hempel, D.M., Roberts, B.L., St George, J.A., and Kaplan, J.M. (2004). Enhanced efficacy of melanoma vaccines in the absence of B lymphocytes. *J. Immunother.* 27, 273–281.
- Qin, Z., Richter, G., Schüler, T., Ibe, S., Cao, X., and Blankenstein, T. (1998). B cells inhibit induction of T cell-dependent tumor immunity. *Nat. Med.* 4, 627–630.
- Rauch, P.J., Chudnovskiy, A., Robbins, C.S., Weber, G.F., Etzrodt, M., Hilgendorf, I., Tiglaio, E., Figueiredo, J.L., Iwamoto, Y., Theurl, I., et al. (2012). Innate response activator B cells protect against microbial sepsis. *Science* 335, 597–601.
- Rhee, J.S., Diaz, R., Korets, L., Hodgson, J.G., and Coussens, L.M. (2004). TIMP-1 alters susceptibility to carcinogenesis. *Cancer Res.* 64, 952–961.
- Rhodes, D.R., Yu, J., Shanker, K., Deshpande, N., Varambally, R., Ghosh, D., Barrette, T., Pandey, A., and Chinnaiyan, A.M. (2004). ONCOMINE: a cancer microarray database and integrated data-mining platform. *Neoplasia* 6, 1–6.
- Ruffell, B., Au, A., Rugo, H.S., Esserman, L.J., Hwang, E.S., and Coussens, L.M. (2012). Leukocyte composition of human breast cancer. *Proc. Natl. Acad. Sci. USA* 109, 2796–2801.
- Schioppa, T., Moore, R., Thompson, R.G., Rosser, E.C., Kulbe, H., Nedospasov, S., Mauri, C., Coussens, L.M., and Balkwill, F.R. (2011). B regulatory cells and the tumor-promoting actions of TNF- α during squamous carcinogenesis. *Proc. Natl. Acad. Sci. USA* 108, 10662–10667.
- Shah, S., Divekar, A.A., Hilchey, S.P., Cho, H.M., Newman, C.L., Shin, S.U., Nechustan, H., Challita-Eid, P.M., Segal, B.M., Yi, K.H., and Rosenblatt, J.D. (2005). Increased rejection of primary tumors in mice lacking B cells: inhibition of anti-tumor CTL and TH1 cytokine responses by B cells. *Int. J. Cancer* 117, 574–586.
- Silverman, G.J. (2006). Therapeutic B cell depletion and regeneration in rheumatoid arthritis: emerging patterns and paradigms. *Arthritis Rheum.* 54, 2356–2367.
- Small, E.J., Schellhammer, P.F., Higano, C.S., Redfern, C.H., Nemunaitis, J.J., Valone, F.H., Verjee, S.S., Jones, L.A., and Hershberg, R.M. (2006). Placebo-controlled phase III trial of immunologic therapy with sipuleucel-T (APC8015) in patients with metastatic, asymptomatic hormone refractory prostate cancer. *J. Clin. Oncol.* 24, 3089–3094.
- Tadmor, T., Zhang, Y., Cho, H.M., Podack, E.R., and Rosenblatt, J.D. (2011). The absence of B lymphocytes reduces the number and function of T-regulatory cells and enhances the anti-tumor response in a murine tumor model. *Cancer Immunol. Immunother.* 60, 609–619.
- Tan, T.T., and Coussens, L.M. (2007). Humoral immunity, inflammation and cancer. *Curr. Opin. Immunol.* 19, 209–216.
- Tarella, C., Passera, R., Magni, M., Benedetti, F., Rossi, A., Gueli, A., Patti, C., Parvis, G., Ciceri, F., Gallamini, A., et al. (2011). Risk factors for the development of secondary malignancy after high-dose chemotherapy and autograft, with or without rituximab: a 20-year retrospective follow-up study in patients with lymphoma. *J. Clin. Oncol.* 29, 814–824.
- van Kempen, L.C.L., Rhee, J.S., Dehne, K., Lee, J., Edwards, D.R., and Coussens, L.M. (2002). Epithelial carcinogenesis: dynamic interplay between neoplastic cells and their microenvironment. *Differentiation* 70, 610–623.
- Wansom, D., Light, E., Worden, F., Prince, M., Urba, S., Chepeha, D.B., Cordell, K., Eisbruch, A., Taylor, J., D'Silva, N., et al. (2010). Correlation of cellular immunity with human papillomavirus 16 status and outcome in patients with advanced oropharyngeal cancer. *Arch. Otolaryngol. Head Neck Surg.* 136, 1267–1273.
- Wong, S.C., Puaux, A.L., Chittezhath, M., Shalova, I., Kajiji, T.S., Wang, X., Abastado, J.P., Lam, K.P., and Biswas, S.K. (2010). Macrophage polarization to a unique phenotype driven by B cells. *Eur. J. Immunol.* 40, 2296–2307.

Cancer Cell, Volume 25

Supplemental Information

B Cells Regulate Macrophage Phenotype and Response to Chemotherapy in Squamous Carcinomas

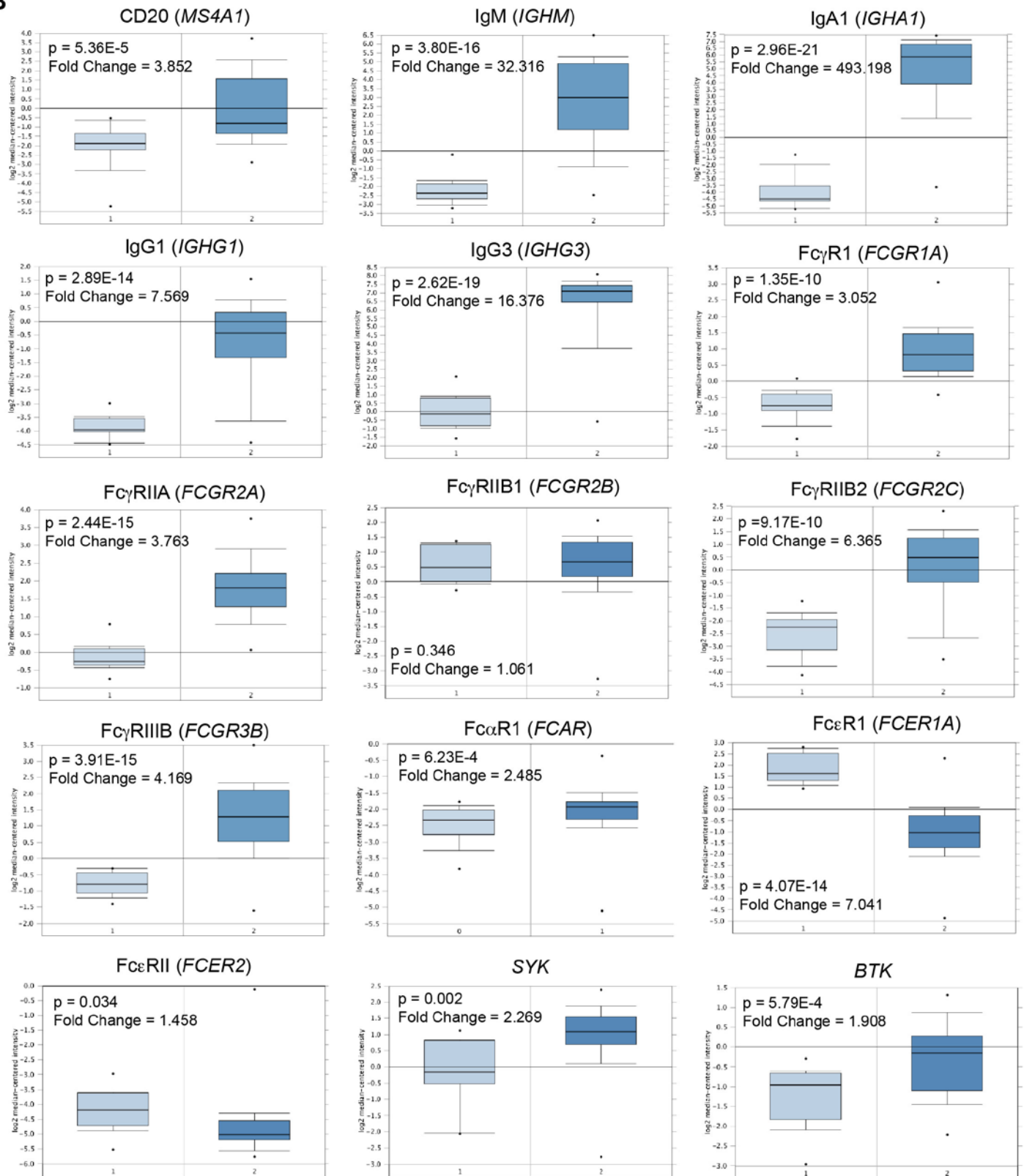
Nesrine I. Affara, Brian Ruffell, Terry R. Medler, Andrew J. Gunderson, Magnus Johansson, Sophia Bornstein, Emily Bergsland, Martin Steinhoff, Yijin Li, Qian Gong, Yan Ma, Jane F. Wiesen, Melissa H. Wong, Molly Kulesz-Martin, Bryan Irving, and Lisa M. Coussens

SUPPLEMENTAL FIGURES

A

		CD20 mRNA Expression			
Type	Type/ Subtype	Fold	n size	p value	
Adrenal	Total	1.0	10/6	NS	
	Pheochromocytoma	0.9	8/5	NS	
Bone	Total	0.9	24/7	NS	
	Chondrosarcoma	1.1	4/7	NS	
Bone Marrow	Total	0.9	9/7	NS	
	ALL/ B-Cell	0.4	55/3	NS	
	ALL/ T-Cell	1.4	13/3	NS	
	AML/ M0	0.4	8/3	NS	
	AML/ M1	0.1	3/3	NS	
	AML/ M2	0.2	5/3	NS	
	AML/ M5	0.1	3/3	NS	
Brain	Total	0.5	4/3	NS	
	Glioblastoma	1.0	19/1097	NS	
Breast	Total	1.0	9/15	NS	
	Oligodendroglioma	0.9	4/15	NS	
	Infiltrating duct and lobular Ca	1.9	113/24	NS	
Breast	Infiltrating ductal Ca, HER2 +	5.0	7/18	*	
	Infiltrating ductal Ca, HER2 -	5.2	10/18	NS	
	Lobular Ca	1.7	62/18	NS	
	Lobular Ca	1.6	9/18	NS	
Cervix	Total	2.7	9/43	**	
	SCC	3.0	5/44	*	
Colorectal	Total	0.3	135/131	NS	
	Rectum	0.2	9/82	NS	
	Cecum/ right ascending colon	0.5	24/82	NS	
	Colon (location unspecified)	0.6	6/82	NS	
	Left descending colon/ sigmoid	0.3	20/82	NS	
	Transverse colon	0.8	4/82	NS	
	Mucinous	0.1	7/82	NS	
Endometrium	Total	0.6	23/82	NS	
	AdenoCa	0.7	52/10	NS	
Esophagus	Total	0.7	24/10	NS	
	Mullerian tumor	0.6	7/10	NS	
Esophagus	Total	4.4	14/8	NS	
	AdenoCa	1.1	9/8	NS	
HNSC	Total	1.1	42/5	NS	
	Larynx	16.6	6/3	NS	
	Parotid gland	19.8	8/3	NS	
	Oropharynx	19.7	18/3	NS	
	Tongue	0.7	3/3	NS	
Kidney	Total	0.7	5/3	NS	
	Adenoid Cys Ca	1.3	67/59	*	
Kidney	Clear cell Ca	1.6	35/45	**	
	Renal cell Ca	1.1	18/45	*	
	Wilms tumors	0.8	4/45	NS	
Liver	Total	1.0	20/27	NS	
	Hepatocellular Ca	1.1	13/27	NS	
Lung	Total	2.5	109/80	***	
	AdenoCa	3.9	17/58	***	
	Previous smoker	3.2	5/58	NS	
	Never smoked	2.9	17/58	NS	
	Current smoker	0.8	3/58	NS	
	Smoking unknown	3.2	5/58	*	
	Large cell Ca	2.6	9/58	NS	
	Non-small cell Ca	0.5	4/58	NS	
Lung	Small cell Ca	4.3	37/58	**	
	SCC	3.6	3/58	NS	
	Poorly differentiated	0.8	4/58	NS	
	Mesothelioma	1.9	142/25	***	
Lymphoid	Total	2.3	6/4	**	
	Mantle cell	1.9	4/4	*	
	Follicular grade 1	1.8	4/4	*	
	Follicular grade 2	1.7	7/4	*	
	Follicular grade 3	1.7	10/4	***	
	Follicular small cleaved cell	1.8	3/4	NS	
	Lymphoblastic, extranodal	1.9	4/4	**	
	Marginal zone, extranodal	1.8	4/4	**	
	Marginal zone, LN	1.7	4/4	NS	
	Diffuse mixed, LN	1.6	30/4	*	
	Diffuse large cell, LN	1.4	5/4	NS	
	Diffuse small lymphocytic	1.2	19/4	NS	
	Diffuse large cell, extranodal	1.1	4/4	NS	
Lymphoid	Diffuse small cleaved cell	0.2	4/4	NS	
	Peripheral T-cell	0.03	7/4	NS	
	Cutaneous T-cell	0.6	13/4	NS	
	Hodgkin's disease	0.9	11/126	NS	
Myometrium	Total	0.9	5/126	NS	
	Leiomyosarcoma	1.1	149/101	**	
Ovary	Total	1.1	37/10	*	
	AdenoCa	1.1	4/10	NS	
	Serous cyst	1.1	4/10	NS	
	Undifferentiated or mixed	1.1	8/10	NS	
	Ascites fluid	1.1	15/10	NS	
	Clear cell	1.0	7/10	NS	
	Mullerian tumor	1.0	3/10	NS	
Pancreas	Total	1.6	41/17	*	
	AdenoCa	5.4	30/17	*	
	IPMN	5.0	5/17	NS	
Prostate	Total	0.8	6/17	NS	
	Islet Cell Ca	0.2	73/27	NS	
Skin	Total	2.5	40/31	*	
	Vulva SCC	15.4	10/31	***	
Small Int	Total	5.3	25/31	*	
	Melanoma	0.7	15/86	NS	
Small Int	Total	2.5	8/37	*	
	AdenoCa	0.7	6/37	NS	
Stomach	Total	5.1	33/33	***	
	Signet ring cell Ca	20.4	3/33	***	
	AdenoCa	8.6	15/33	***	
Testis	Total	0.9	10/33	NS	
	GI stromal tumors	2.9	6/5	**	
Thyroid	Total	2.6	22/12	**	
	Papillary Ca	3.4	3/13	*	
	Papillary/ Follicular Ca	1.9	8/13	NS	
Urinary	Total	1.0	3/13	NS	
	Follicular Ca	1.0	25/7	NS	

		Ig mRNA Expression			
Type	Type/ Subtype	Fold	n size	p value	
Adrenal	Total	1.6	10/6	NS	
	Pheochromocytoma	1.8	8/5	NS	
Bone	Total	0.4	24/7	NS	
	Chondrosarcoma	0.5	4/7	NS	
Bone Marrow	Total	0.3	9/7	NS	
	ALL/ B-Cell	0.05	55/3	NS	
	ALL/ T-Cell	0.04	13/3	NS	
	AML/ M0	0.04	8/3	NS	
	AML/ M1	0.4	3/3	NS	
	AML/ M2	0.4	5/3	NS	
	AML/ M5	0.2	3/3	NS	
Brain	Total	0.1	4/3	NS	
	Glioblastoma	2.2	19/1097	***	
Brain	Oligodendroglioma	9.9	9/15	***	
	Infiltrating duct and lobular Ca	0.9	4/15	NS	
	Infiltrating ductal Ca, HER2 +	2.9	113/24	**	
Breast	Infiltrating ductal Ca, HER2 -	6.2	7/18	**	
	Lobular Ca	2.3	10/18	NS	
	Lobular Ca	2.0	62/18	*	
	Lobular Ca	0.9	9/18	NS	
Cervix	Total	2.7	10/44	**	
	SCC	3.0	5/44	*	
Colorectal	Total	1.8	135/131	***	
	Rectum	2.4	9/82	**	
	Cecum/ right ascending colon	2.3	24/82	***	
	Colon (location unspecified)	1.9	6/82	**	
	Left descending colon/ sigmoid	1.9	20/82	**	
	Transverse colon	1.4	4/82	NS	
	Mucinous	1.0	7/82	NS	
Endometrium	Total	1.9	23/82	***	
	AdenoCa	3.2	52/10	NS	
Esophagus	Total	3.4	24/10	NS	
	Mullerian tumor	0.4	7/10	NS	
Esophagus	Total	3.3	14/8	***	
	AdenoCa	3.5	9/8	**	
HNSC	Total	6.4	42/5	NS	
	Larynx	11.5	6/3	*	
	Parotid gland	11.9	6/3	*	
	Oropharynx	9.6	19/3	*	
	Tongue	3.1	4/3	*	
Kidney	Total	1.5	5/3	NS	
	Adenoid Cys Ca	2.0	68/59	**	
Kidney	Clear cell Ca	2.7	35/45	***	
	Renal cell Ca	0.9	18/45	NS	
	Wilms tumors	0.4	4/45	NS	
Liver	Total	2.9	20/27	NS	
	Hepatocellular Ca	2.3	13/27	NS	
Lung	Total	1.8	109/80	***	
	AdenoCa	2.4	17/58	***	
	Previous smoker	1.5	5/58	NS	
	Never smoked	2.5	17/58	NS	
	Current smoker	1.5	3/58	NS	
	Smoking unknown	2.4	5/58	**	
	Large cell Ca	2.3	9/58	**	
	Non-small cell Ca	1.4	4/58	NS	
Lung	Small cell Ca	2.3	37/58	**	
	SCC	2.3	3/58	NS	
	Poorly differentiated	0.9	4/58	NS	
	Mesothelioma	0.2	143/25	NS	
Lymphoid	Total	0.2	6/4	NS	
	Mantle cell	0.3	4/4	NS	
	Follicular grade 1	0.3	4/4	NS	
	Follicular grade 2	0.3	4/4	NS	
	Follicular grade 3	0.2	7/4	NS	
	Follicular small cleaved cell	0.1	10/4	NS	
	Lymphoblastic, extranodal	0.4	3/4	NS	
	Marginal zone, extranodal	0.2	4/4	NS	
	Marginal zone, LN	0.2	4/4	NS	
	Diffuse mixed, LN	0.1	4/4	NS	
	Diffuse large cell, LN	0.1	30/4	NS	
	Diffuse small lymphocytic	0.3	5/4	NS	
	Diffuse large cell, extranodal	0.1	19/4	NS	
Lymphoid	Diffuse small cleaved cell	0.5	4/4	NS	
	Peripheral T-cell	0.5	4/4	NS	
	Cutaneous T-cell	0.4	7/4	NS	
	Hodgkin's disease	0.7	13/4	NS	
Myometrium	Total	1.1	11/126	NS	
	Leiomyosarcoma	3.7	5/126	**	
Ovary	Total	1.5	149/101	NS	
	AdenoCa	2.7	37/10	NS	
	Serous cyst	3.2	4/10	NS	
	Undifferentiated or mixed	0.07	4/10	NS	
	Ascites fluid	0.2	8/10	NS	
	Clear cell	0.3	15/10	NS	
	Mullerian tumor	0.1	7/10	NS	
Pancreas	Total	11.4	45/17	**	
	AdenoCa	6.8	33/17	***	
	IPMN	3.7	5/17	NS	
Prostate	Total	1.0	6/17	NS	
	Islet Cell Ca	0.8	73/27	NS	
Skin	Total	16.9	41/31	***	
	Vulva SCC	5.6	11/31	***	
Small Int	Total	2.5	26/31	**	
	Melanoma	2.2	15/86	**	
Small Int	Total	5.2	8/37	**	
	AdenoCa	0.5	6/37	NS	
Stomach	Total	4.4	35/33	***	
	Signet ring cell Ca	8.3	3/33	***	
	AdenoCa	6.0	15/33	***	
Testis	Total	1.0	10/33	NS	
	GI stromal tumors	15.1	6/5	NS	
Thyroid	Total	4.9	25/13	NS	
	Papillary Ca	15.4	3/13	*	
	Papillary/ Follicular Ca	5.1	8/13	NS	
Urinary	Total	0.08	3/13	NS	
	Follicular Ca	2.7	25/7	NS	

B

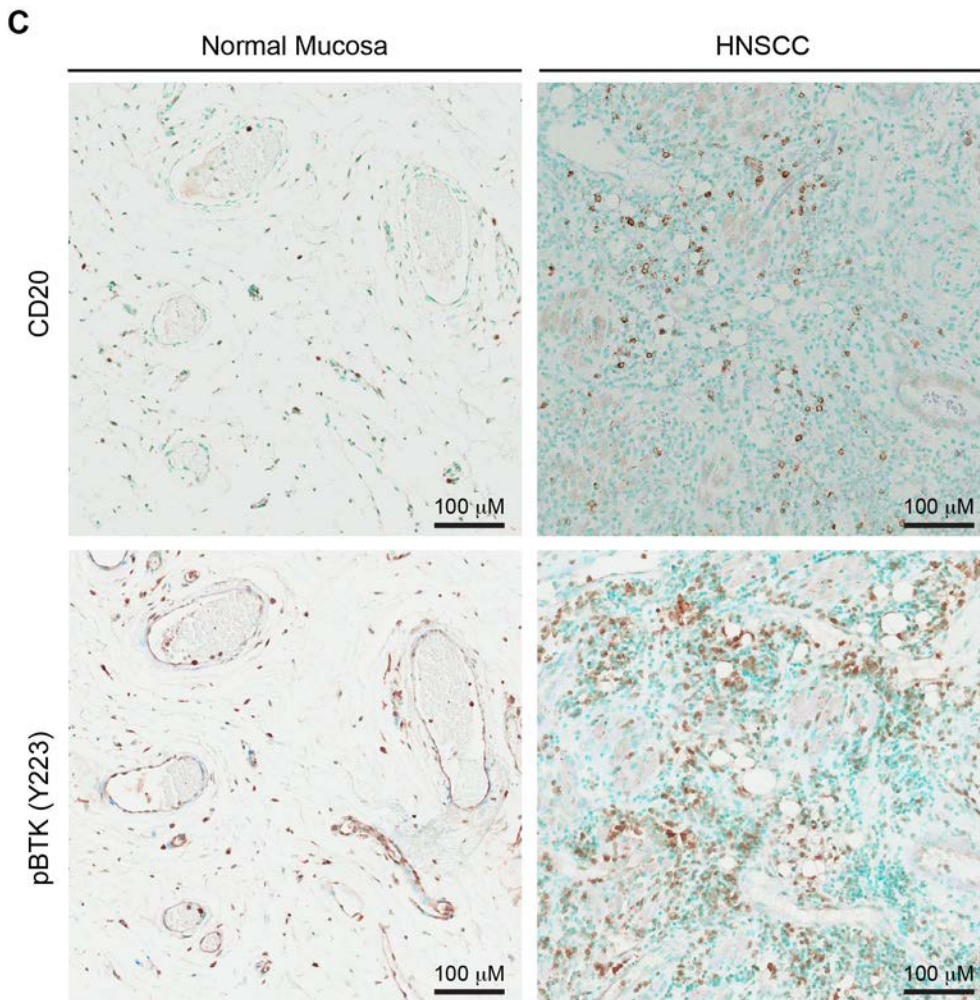
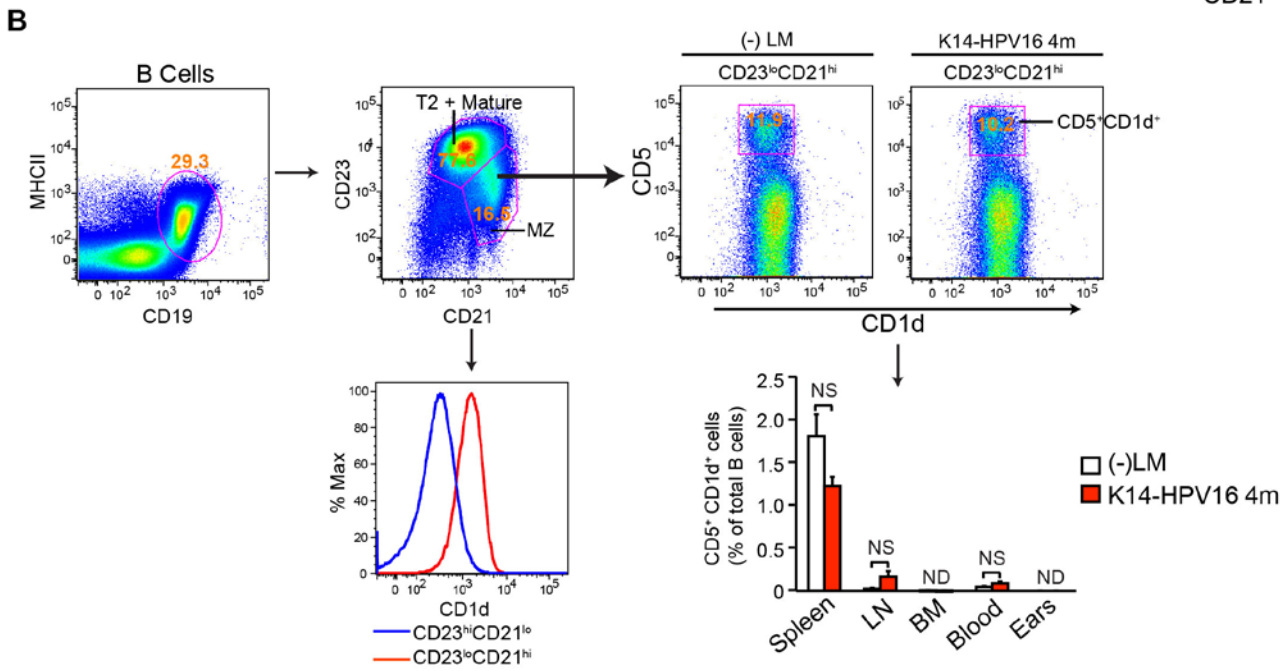
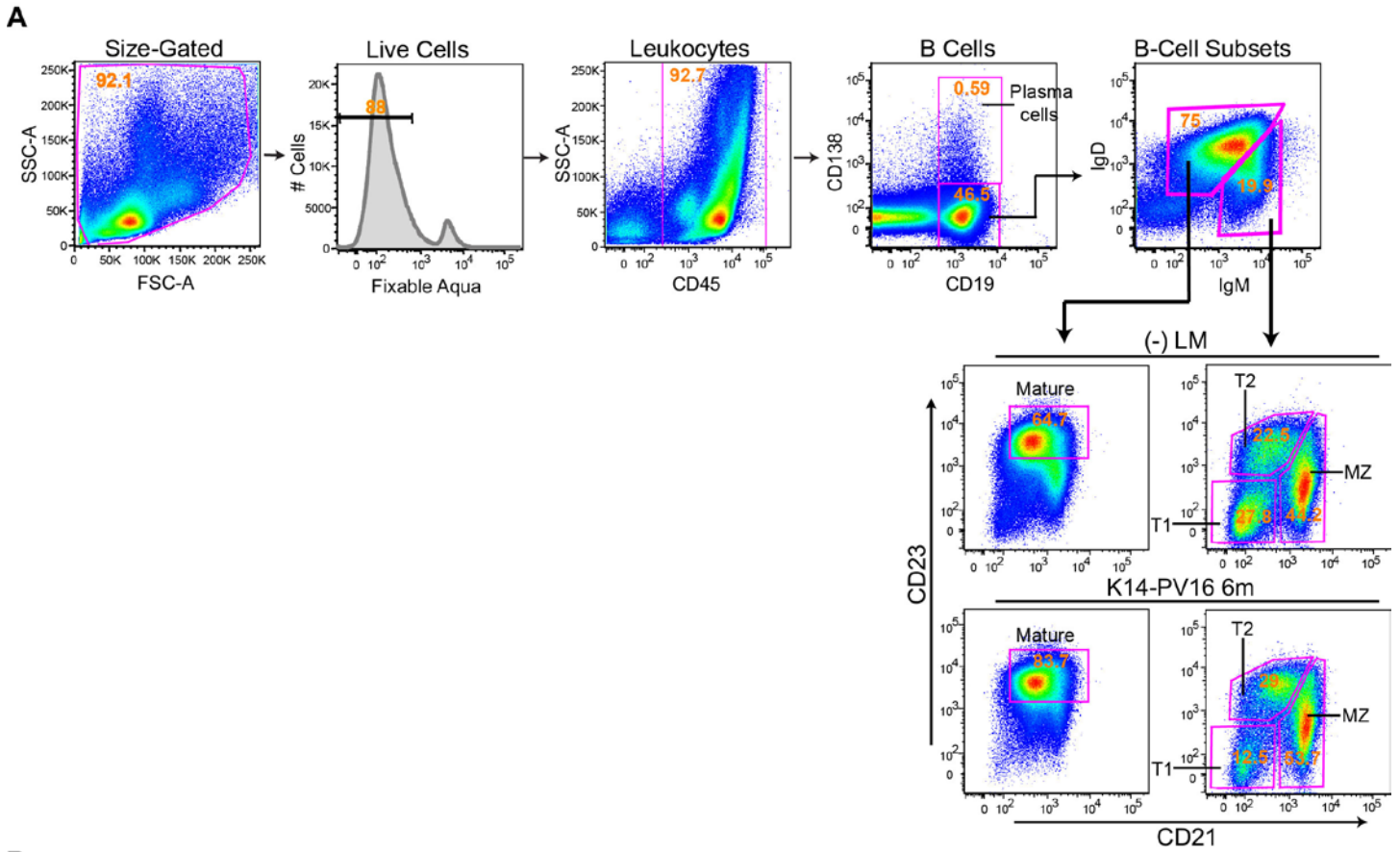
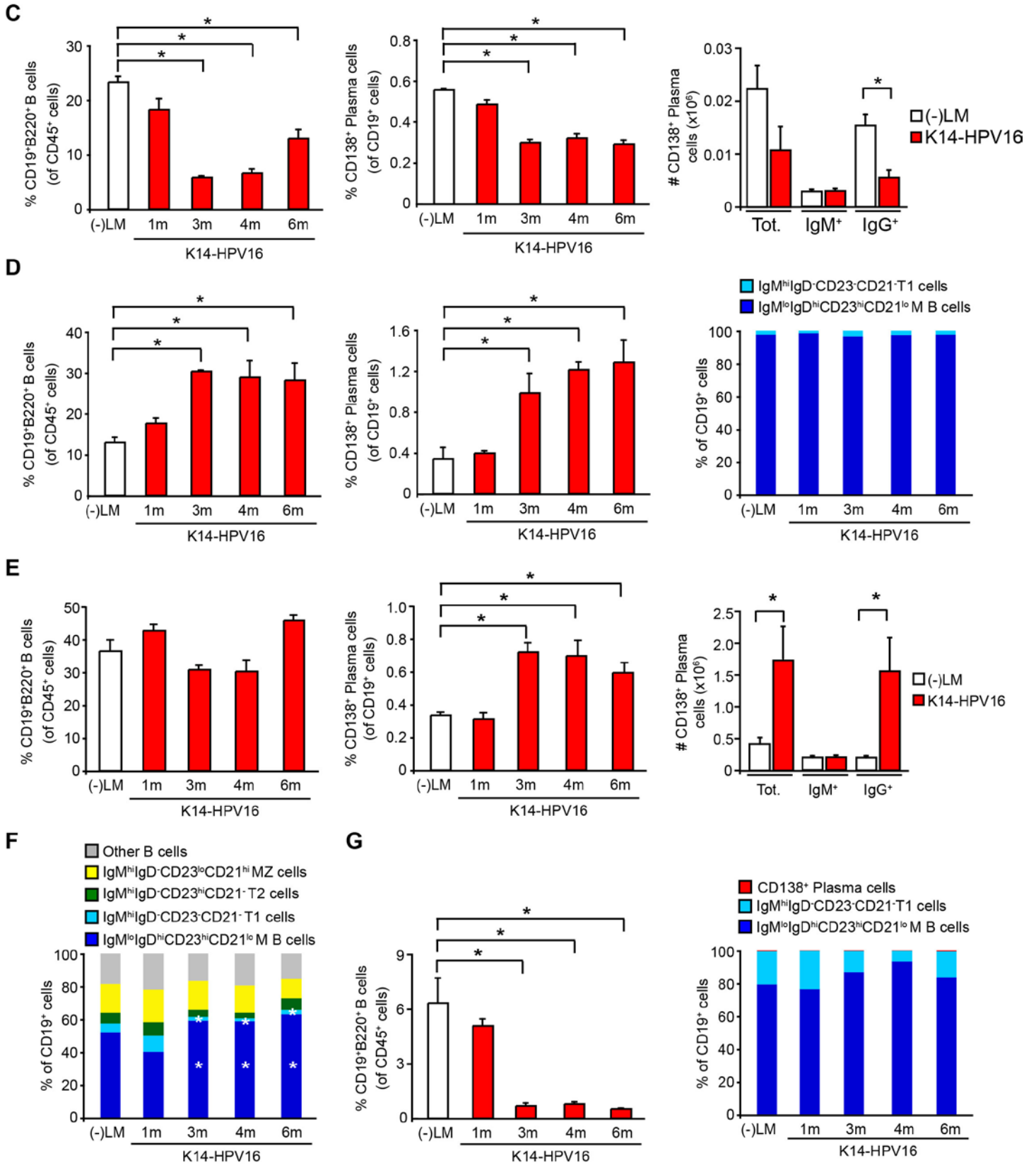


Figure S1, related to Figure 1. (A) Tables depicting subtypes of human cancers wherein CD20 and Ig mRNA levels were assessed using Affymatrix Human U133 Plus 2 microarrays, respectively. Data represent median fold change of CD20 or Ig mRNA levels in cancer tissue as compared to corresponding normal tissue. $p < 0.05$, $**p < 0.01$, $***p < 0.001$ indicates statistically significant differences between cancer tissue and normal control tissue by Wilcoxon rank-sum test. n , depicts number (n) of cancer tissue / number of normal tissue. Ca, carcinoma; HNSC, head and neck squamous carcinoma; GI, gastrointestinal; SCC, squamous cell carcinoma; LN, lymph node; Int, intestine. (B) Relative expression comparing normal buccal mucosa ($n=13$) and HNSCC ($n=41$) from the Ginos Head-Neck dataset analyzed via Oncomine. “Normal” tissue is shown to the left in each graph and is denoted with a ‘1’. Tumor tissue is shown to the right in each graph and is denoted with a ‘2’. p values were determined by a Student’s t test. (C) Representative IHC showing CD20⁺ and phosphorylated BTK⁺ (pBTK; Y223) cells in adjacent human tissue sections of “normal” mucosa and HNSCC.





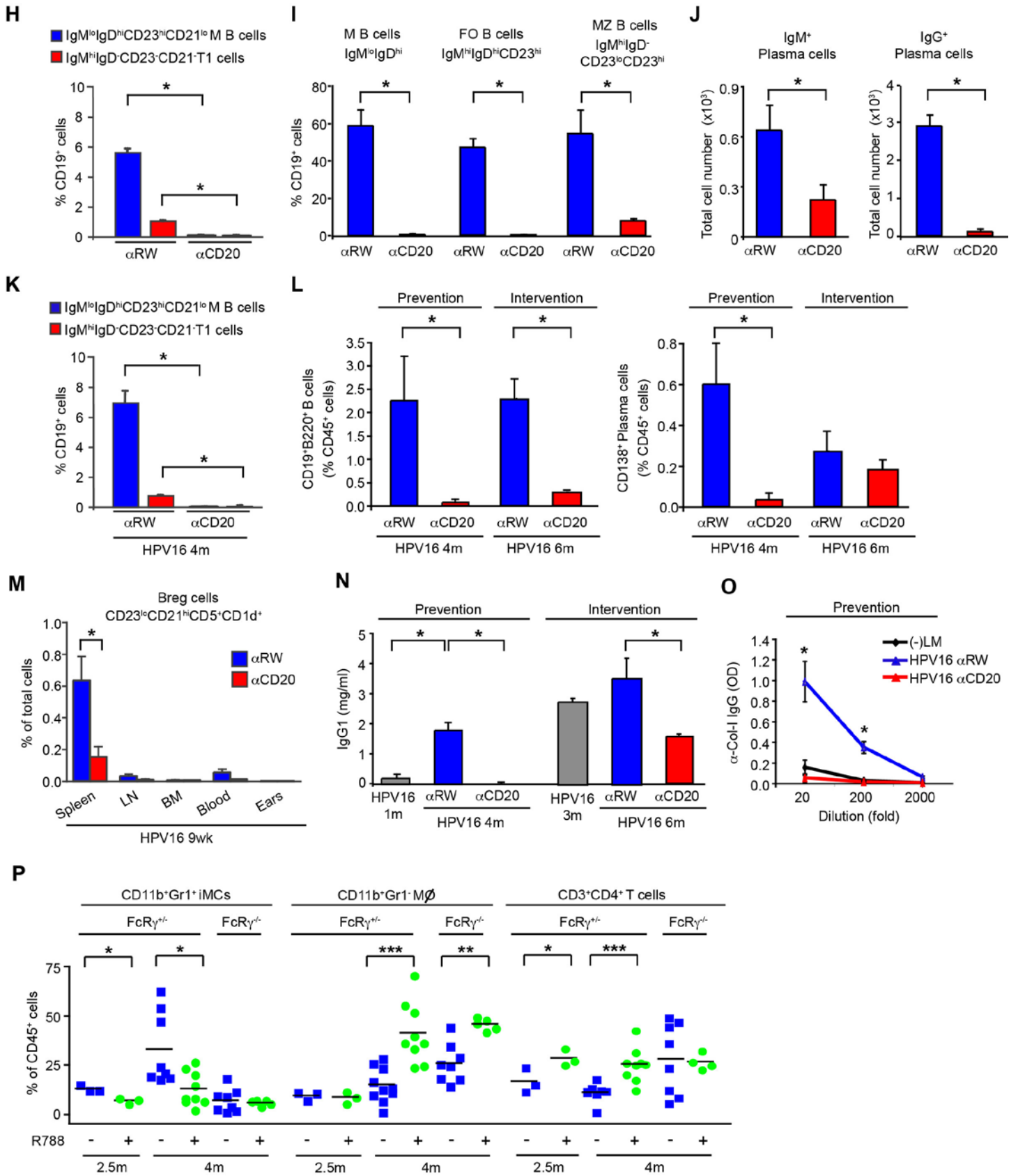


Figure S2, related to Figure 2. (A) B cell subsets in spleen of K14-HPV16 mice at 6 month of age versus age-matched negative littermates (-LM) as evaluated by flow cytometry. CD21 and CD23 were used to delineate Transitional 1 (T1; IgM^{hi}IgD⁻CD23⁻CD21⁻), T2 (IgM^{hi}IgD⁻CD23^{hi}CD21⁻), MZ (IgM^{hi}IgD⁻CD23^{lo}CD21^{hi}), and mature (M) follicular B cells (IgM^{lo}IgD^{hi}CD23^{hi}CD21^{lo}). (B) B regulatory cells were characterized as a B cell subset derived from splenic MZ B cells (CD23^{lo}CD21^{hi}) expressing high levels of CD5 and CD1d (CD19⁺MHCII⁺CD23^{lo}CD21^{hi} CD5^{hi}CD1d^{hi}). Data represent mean \pm SEM (≥ 4 mice/group). (C-G) B cell subsets were assessed in lymphoid organs of negative littermates (-LM) and K14-HPV16 mice at 1, 4, and 6 months of age including (C) bone marrow, (D) lymph nodes (LN), (E-F) spleen, and (G) peripheral blood via flow cytometry. Total B cells were identified using CD19 and B220, while CD138 was used to delineate plasma B cells. Data represent mean \pm SEM (≥ 3 mice/group). Statistical significance was determined via an unpaired *t*-test with **p* < 0.05. (H) Evaluation of B cell subsets in K14-HPV16 mice (5-weeks of age), 7-days following administration of α CD20 mAb (versus control α RW mAb) showing reductions in circulating mature (M) and transitional 1 (T1) B cells in blood. (I-J) Evaluation of B cell subsets in K14-HPV16 mice (2-months of age), 7-days following administration of α CD20 mAb (versus control α RW mAb) showing reductions in mature (M), follicular (FO), and Marginal zone (MZ) B cells in spleen (I) and plasma cells in bone marrow (J). (K) Evaluation of B cell subsets in peripheral blood of K14-HPV16 mice (4 months of age) 7-days following α CD20 mAb (versus control α RW mAb) treatment. (L) Evaluation of B cell subsets in end-stage K14-HPV16 mice enrolled in prevention and intervention trials showing percentages of CD19⁺CD20⁺ B cells and CD138⁺ plasma B cells in bone marrow. (M) Levels of B regulatory cells, identified as CD19⁺MHCII⁺CD23^{lo}CD21^{hi}CD5^{hi}CD1d^{hi}, were significantly reduced in spleens of K14-HPV16 mice following 5 weeks of α CD20. Levels of circulating IgG1 (N) and anti-collagen-I (Col-I) IgG (O) in peripheral blood as assessed by ELISA in K14-HPV16 mice enrolled in prevention and/or intervention trials. Data represent mean \pm SEM (≥ 5 mice/group). Statistical significance was determined via an unpaired *t*-test with **p* < 0.05. (P-Q) Infiltration of CD11b⁺Gr1⁺ immature myeloid cells (iMC), CD11b⁺Gr1⁻ macrophages, and CD3⁺CD4⁺ T lymphocytes in HPV16 skin premalignant tissue as assessed by flow cytometry following treatment with α CD20 or fostamatinib (R788). (R) Mast cell infiltration (blue staining) as assessed quantitatively by chloroacetate esterase IHC in five high-power fields of view per skin tissue following treatment of HPV16 mice with α CD20 or fostamatinib. Solid red line, epidermal-dermal interface; e, epidermis; d, dermis. Scale bars represent 50 μ m. (S) Presence of Gr-1⁺ cells in skin tissue as assessed by automated counting following treatment of HPV16 mice with fostamatinib. Data represent the mean with ≥ 3 mice/group. Statistical significance was determined via an unpaired *t*-test with **p* < 0.05, ***p* < 0.01, ****p* < 0.001. (T) IL-3-dependent bone marrow-derived mast cells (BMDC) were generated from FcR γ ^{+/-} and FcR γ ^{-/-}

mice were stimulated with monoclonal anti-Fc γ RII/III (clone 2.4G2) followed by cross-linking of Fc γ Rs with F(ab'2) anti-rat IgG (25 μ g/ml) (Fc γ R-stim.). Alternatively, BMMC were incubated with circulating Ig-IC from serum isolated from negative littermates (IgG_{WT}) or HPV16 (IgG_{HPV16}) (30 μ g/ml) in the presence or absence of the mast cell stabilizer cromolyn (10 μ M) or Syk inhibitor, R406 (1.0 nM). Levels of IL4, TGF β , TNF α , IL23, IL9, and vascular endothelial growth factor (VEGF) in conditioned medium were assessed by ELISA. Assays were performed in triplicate and a representative analysis from three independent experiments is shown. Statistical significance was determined via an unpaired *t*-test with **p* < 0.05.

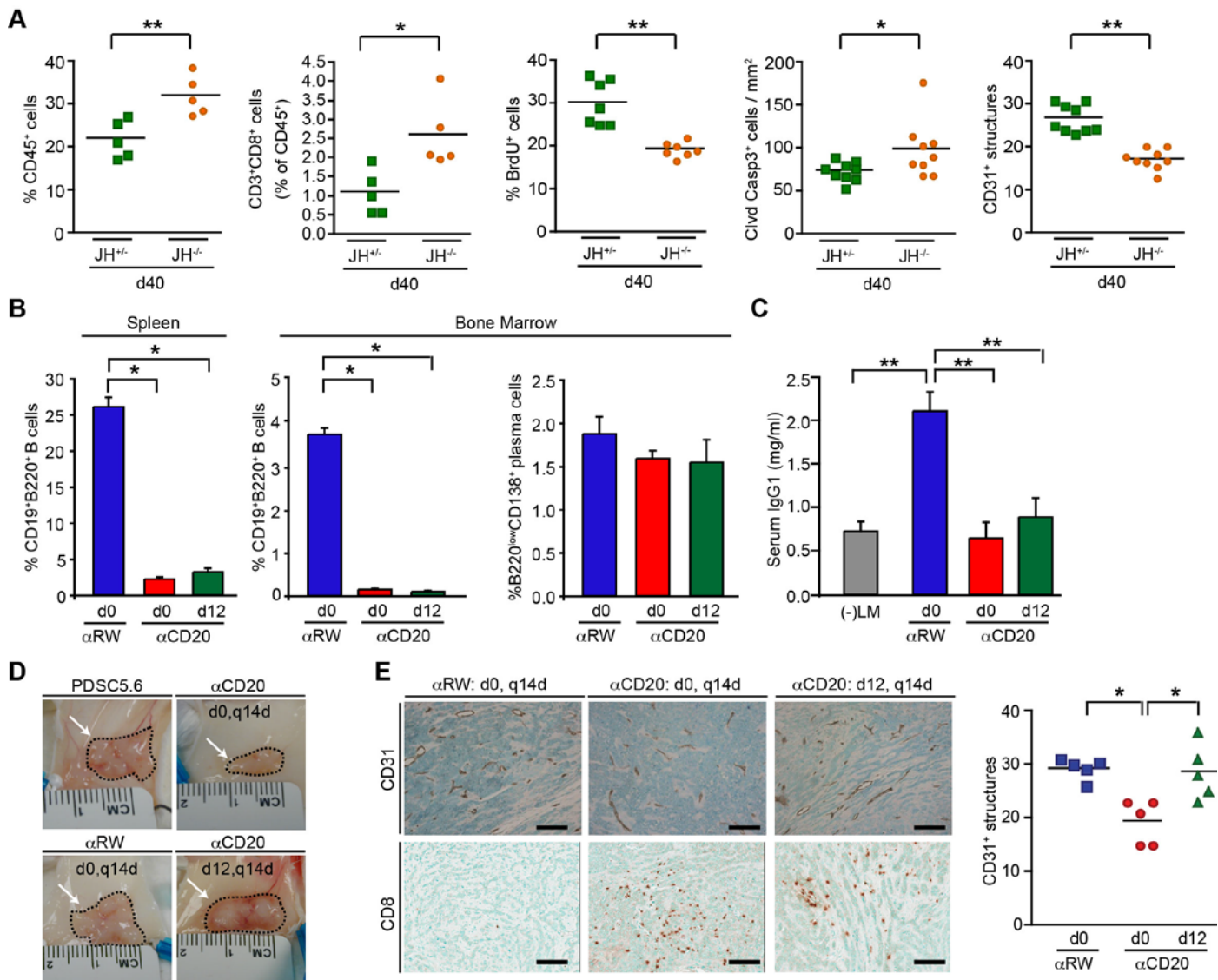


Figure S3, related to Figure 3. (A) Percentages of CD45⁺ cells and CD8⁺ T cells as assessed by flow cytometry, and quantitation of BrdU⁺ cells, cleaved caspase 3⁺ cells and angiogenic vasculature in orthotopic

tumors derived from PDSC5.6 cells growth in syngeneic JH^{+/+} versus JH^{-/-} mice evaluated 40 days following tumor cell inoculation. **(B)** Characterization of CD19⁺B220⁺ B cells in spleen (left panel) and bone marrow (middle panel) from PDSC5.6 tumor bearing syngeneic/n mice, as assessed by flow cytometry, showing percent of B220^{lo}CD138⁺ plasma cells in spleen (left) and bone marrow (right panel) following α CD20 mAb (versus α RW mAb) treatment. **(C)** Circulating IgG levels following α CD20 mAb (versus α RW mAb) treatment as evaluated by ELISA in PDSC5.6 tumor bearing syngeneic/n mice. Data represent mean \pm SEM (≥ 10 mice/group). **(D)** Representative images of PDSC5.6-derived SCCs 48 day after implantation. **(E)** Representative micrographs showing CD31⁺ vessels (top panels, brown staining) and CD8⁺ T lymphocytes (bottom panels, brown staining); scale bar, 50 μ m. Quantitation of vessels in PDSC5.6-derived SCCs (shown on right) as evaluated by five high-power fields of view per tumor. d0 (day 0) depicts time of PDSC5.6 tumor cell inoculation while d12 (day 12) indicates appearance of visible tumors. Statistical significance was determined via an unpaired *t*-test with **p* < 0.05, ***p* < 0.01.

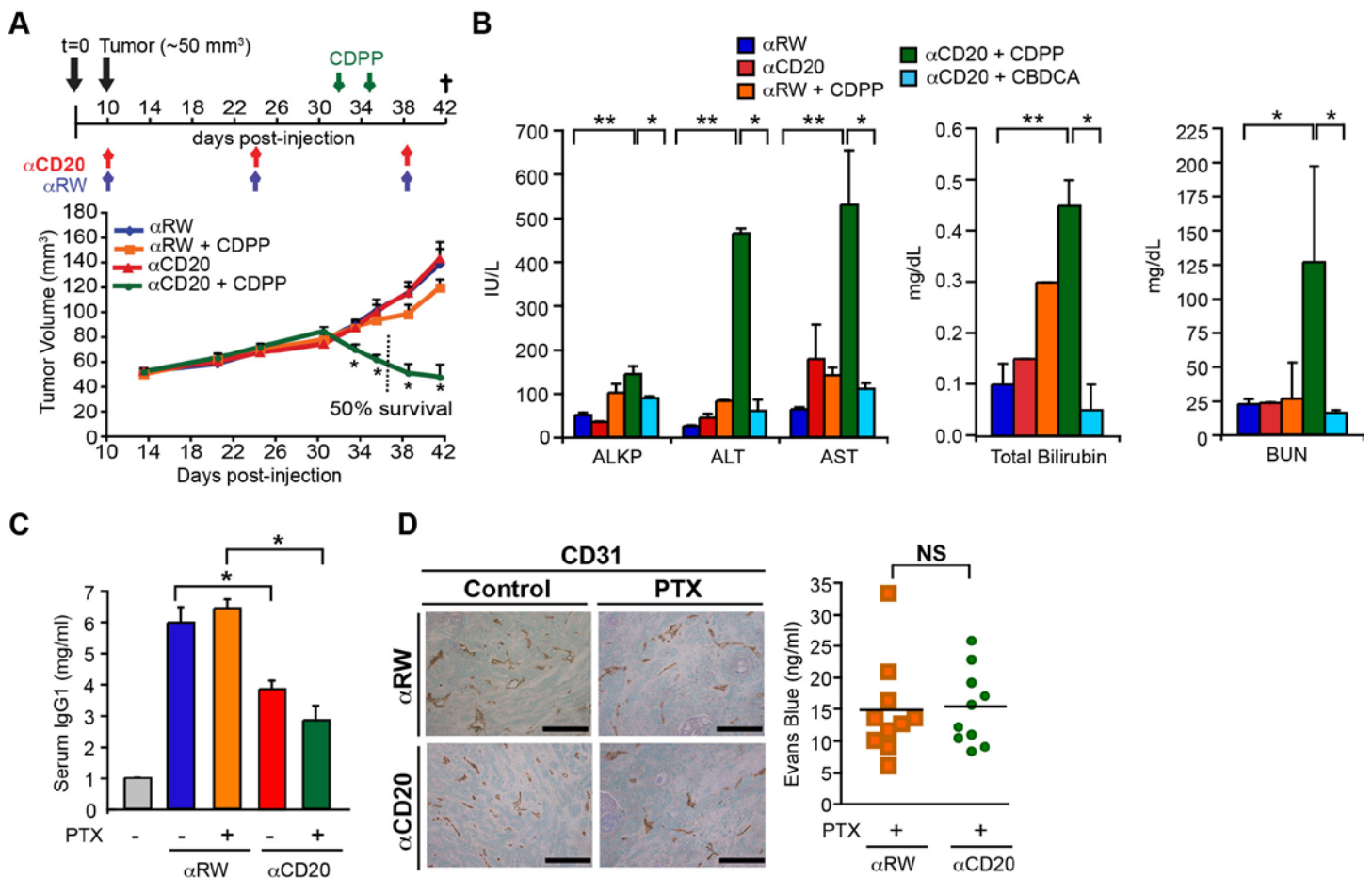
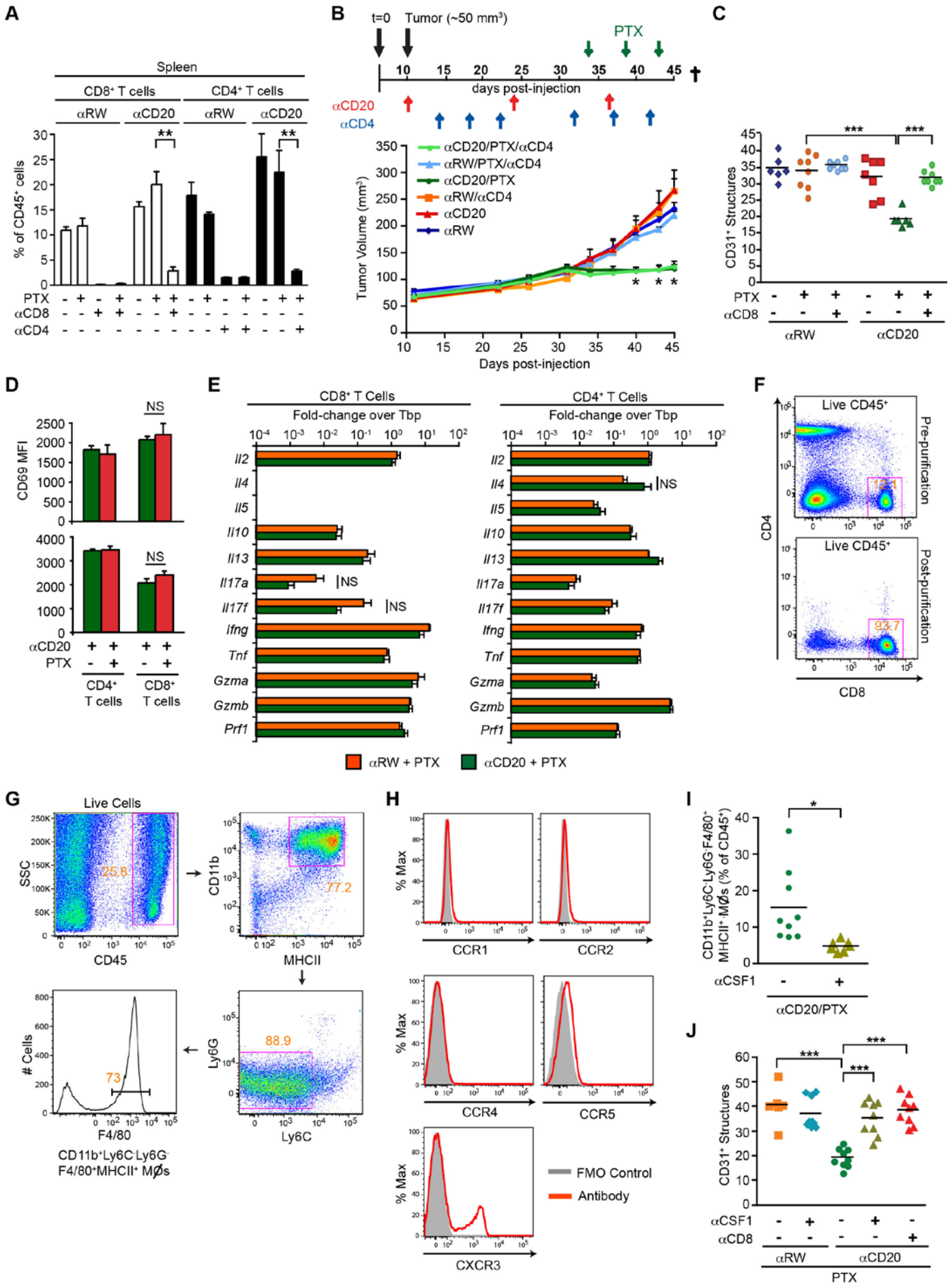


Figure S4, related to Figure 4. (A) Growth of PDSC5.6 SCCs in syngeneic mice receiving α CD20 or α RW mAbs at the time of visible tumor appearance (d10), followed 3 weeks later by administration of carboplatin

(CBDCA; 50 mg/kg; q4dx3) (5-10 mice per group). **(B)** Evaluation of acute liver and renal toxicity in FVB/n mice harboring orthotopic SCCs that received α CD20 or α RW mAb at the time of visible tumor appearance (d10), followed 3 weeks later by administration of the platinum-containing chemotherapeutic agents Cisplatin (CDPP; 10 mg/kg; q4dx2) or Carboplatin (CBDCA; 50 mg/kg; q5dx3). Liver toxicity as evaluated by alkaline phosphatase (ALKP), alanine aminotransferase (ALT), aspartate aminotransferase (AST), and total bilirubin; and renal toxicity evaluated by blood urea nitrogen (BUN) and creatinine. Data represent mean \pm SEM (\geq 5 mice/group). **(C)** Representative images depicting PDSC5.6-derived SCCs 45 days following tumor cell inoculation of syngeneic mice treated with α CD20 or α RW mAb starting on day 12 following inoculation (d12), and administration of Paclitaxel (PTX; 12 mg/kg; q4dx3) 3 weeks later. ELISA was performed to assess levels of circulating IgG in blood at d45 following treatment with α CD20 or α RW mAb in the presence or absence of PTX. Data represent mean \pm SEM (\geq 5 mice/group). **(D)** Representative IHC of CD31⁺ vessels (brown staining) in PDSC5.6 tumor tissue. Mice were also evaluated for vascular leakage using the Miles assay. Data depicts quantitative evaluation of Evans blue dye leakage into interstitial tissue of PDSC5.6 tumors. Scale bar; 100 μ m. NS, not statistically significant. Statistical significance was determined via an unpaired *t*-test with **p* < 0.05, ***p* < 0.01.



PRF1, *GZMA*, *GZMB*, and *CD69* using OncoPrint coexpression heat maps and the Ginos Head-Neck dataset. Columns represent individual patient samples. Correlation is derived from average linkage hierarchical clustering. Data is displayed as log₂ median-centered intensity with lowest expression in blue and highest expression in red.

SUPPLEMENTAL EXPERIMENTAL PROCEDURES

Histology

Percentages of dysplastic skin was determined following histological evaluation of H&E-stained and panKeratin IHC skin as previously described (Coussens et al., 1996). Briefly, by 1-mo of age, 100% of K14-HPV16 mice develop hyperplastic lesions characterized by marked expansion of the basal and granular layers. Despite these changes, the process of terminal differentiation is preserved, as evidenced by prevalence of dense cytoplasmic keratohyalin granules and presence of upper most non-nucleated eosinophilic cornified cells. Progression of hyperplastic lesions into dysplasia at 4-mo of age is accompanied with loss of terminal differentiation, as revealed by parakeratosis characterized by retention of nuclei in the stratum corneum. Values represent percentages of high-power fields of view of dysplastic lesions compared to whole ear skin per mouse and 5-10 mice per category.

Immunohistochemistry

Tissue samples were immersion-fixed in 10% neutral-buffered formalin followed by dehydration through graded series of alcohols and xylene and embedded in paraffin as previously described (Andreu et al., 2010). Tissue sections were deparaffinized using xylene and rehydrated through a graded series of alcohol. To identify proliferating cells in tissue sections, mice received intraperitoneal injections of bromodeoxyuridine (BrdU; Roche Diagnostics) dissolved in PBS (50 mg/g of mouse body weight) 90 min prior to sacrifice. Tissue sections were subjected to antigen retrieval by steam heating in Citra™ antigen retrieval solution (BioGenex) or proteinase K (Dako). Sections were then incubated with blocking buffer containing 5.0% goat serum (Thermo Fisher) and 2.5% bovine serum albumin (BSA), followed by primary antibody incubation, e.g., rat anti-BrdU (MCA2060; Serotec), rat anti-mouse PECAM1/CD31 (BioLegend), rat anti-Gr1 (eBiosciences), rat anti-mouse cleaved capsase 3 (Cell Signaling), or rabbit anti-mouse CD8 (Novus Biologicals). Tissue sections were then incubated with the corresponding biotinylated secondary antibodies (1:200, Vector Laboratories), washed, and incubated with horseradish peroxidase conjugated avidin complex (ABC Elite, Vector Laboratories) for 30 min, followed by incubation with Fast 3,3 diaminobenzidine (DAB, Vector Laboratories). Tissue sections were counterstained with methyl green, dehydrated, and mounted with Cytoseal 60 (Thermo Fisher).

To visualize serine esterase activity in mast cells, chloroacetate esterase (CAE) histochemistry was performed as previously described (Coussens et al., 1999). Briefly, 1.0 mg of naphthol AS-D chloroacetate (Sigma) was dissolved in 20 ml of N, N-dimethyl formamide (DMF) and 1.0 ml buffer (8% DMF, 20% ethylene glycol monoethylether in 80mM Tris-maleate pH 7.5). The resulting solution was subsequently added to 1.0 mg of Fast Blue BB salt (Sigma) and applied to tissue sections. Sections were then dehydrated and mounted in glycerol. Photomicrographs were captured at high-magnification (40X) on a Leica DM-RXA

microscope attached to a Leica digital camera (Leica Microsystem) operated by OpenLab software™ (Improvision).

Quantitative analysis of immune cells and angiogenesis was performed by counting cells and CD31⁺ vascular structures in at least five high-power fields (40X) per age-matched tissue section (n ≥ 5 mice per group), or by automated image acquisition using the Aperio ScanScope CS Slide Scanner (Aperio Technologies) system with a 20x objective to capture whole slide digital images. Nuclear or membrane default algorithms (Aperio) were used to assess positive staining.

Real-time PCR

Mice were cardiac-perfused with PBS to clear peripheral blood. Transplantable tumor tissues were snap-frozen and pulverized in liquid nitrogen for whole tissue analysis, or were used to purify immune populations by fluorescence-activated cell sorting. Total mRNA was prepared using RNeasy Micro/Mini kit guidelines (Qiagen). Contaminating DNA was removed with DNase I (Invitrogen), followed by RNA quantitation using a NanoDrop ND-1000 (Thermo Fisher Scientific). SuperScript III (Invitrogen) was used to reverse transcribe purified RNA into cDNA according to manufacturers directions. Real-time PCR for gene expression was performed using the TaqMan system (Applied Biosystems) with a preamplification step employed during analysis of FACS-sorted populations. The comparative threshold cycle method was used to calculate fold change in gene expression, which was normalized to TATA-binding protein (*Tbp*) as a reference gene.

Flow cytometry and fluorescence-activated cell sorting

Single-cell suspensions were prepared from ear skin, tumor tissues, lymph nodes, spleens, bone marrow and blood as follows: Ear skin or tumor tissues from PBS-perfused mice was manually minced using scissors, followed by a 30 min enzymatic digestion with 2.0 mg/ml collagenase A (Roche), 1.0 mg/ml Hyaluronidase (Worthington), and 50 U/ml DNase I (Roche) in serum-free Dulbecco's modified eagles medium (DMEM) (Invitrogen) at 37°C using continuous stirring conditions. Single cell suspensions from ear or tumor digests, lymph nodes, or spleens were prepared by passing tissue through 70-µm nylon strainers (BD Biosciences). Bone marrow cells were flushed out of femurs using a 23-gauge needle. Blood samples were acquired through cardiac puncture with a heparanized 25-gauge needle, followed by erythrocyte lysis with BD PharmLyse (BD Biosciences).

To prevent non-specific binding, cells were incubated for 30 min at 4°C with rat anti-mouse CD16/CD32 mAb (1:250, BD Bioscience) in PBS also containing Live/Dead Aqua stain (1:250; Invitrogen) to delineate between viable and dead cells. Subsequently, cells were incubated for in PBS containing 1.0 % BSA (Sigma; PBS/BSA) and 2 mM EDTA for 30 min with 100 µl of fluorophore-conjugated anti-mouse antibodies; CD45

(30-F11), CD3e (145-2C11), CD69 (H1.2F3), CD4 (L3T4), CD44 (IM7), CD62L (MEL-14), CD25 (PC61.5), CD8e (53-6.7), CD127 (A7R34), $\gamma\delta$ TCR (GL3), NK1.1 (PK136), CD49b (DX5), CD19 (6D5), B220 (RA3-6B2), CD22 (2D6), CD138 (281-2), CD11b (M1/70), CD11c (N418), MHCII (M5/114.15.2), CD80 (16-10A1), Ly6C (HK1.4), Ly6G (1A8), F4/80 (BM8), CD206 (MR5D3), IgD (11-26c), IgM (II/41), CD21/CD35 (4E3), CD23 (B3B4), CD138 (281-2) CD1d (K253), CD5 (53-7.3) (eBioscience or Biolegend). Cells were then washed once in PBS/BSA/EDTA, followed by fixation with BD Cytotfix for 30 min on ice. After a final wash, cells were stored at 4°C until data acquisition on a LSRII using FACSDiva software (BD Biosciences). Analysis was performed using FlowJo software program (Tree Star Inc).

For fluorescence-activated cell sorting (FACS), cells were prepared as described above without fixation, and sorting was performed on a FACS Aria using CellQuestPro software (BD Biosciences). Single cell suspensions from pancreatic tumors were maintained in 0.1% trypsin inhibitor buffers at all times. Sorted CD11b⁺Ly6C⁻Ly6G⁻F4/80⁺MHCII⁺ macrophages were either seeded at 5.0x10⁴ cells/650 μ l in DMEM containing 0.1% BSA onto 24-well plate and used to collect conditioned medium 12 hr later or flash frozen as a cell pellet for subsequent gene expression analysis. Cell sorted CD3⁺CD4⁺ and CD3⁺CD8⁺ T cells were also used for gene expression analyses.

CD8⁺ T cell chemotaxis assay

CD8⁺ T cells were purified from spleens of naïve FVB/n mice via negative selection using a mouse CD8⁺ T cell enrichment kit according to manufacturers' specifications (StemCell Technologies). Enriched CD8⁺ T cells were seeded (2.5x10⁵ cells/100 μ l DMEM containing 0.1% BSA) on the top chamber of transwell filters (3.0 μ m; Corning), which were subsequently placed in a 24-well plate containing conditioned medium isolated from FACS-sorted macrophages. For some conditions, enriched CD8⁺ T cells were pre-incubated for 15 min on ice with anti-mouse CCR5 (10 μ g/ml; BD Pharminogen) or anti-mouse CXCR3 (10 μ g/ml; BioLegend) prior to seeding into top chambers. 4 hrs following incubation, medium in the lower chamber was collected and analyzed by flow cytometry to count cell numbers using Accuri C6 (Accuri Cytometers).

ELISA

To isolate serum, blood was collected by cardiac puncture and left at room temperature for 2.0 hr for coagulation, then centrifuged at 2000 rpm for 15 min. Serum was then separated and stored at -80°C. Anti-collagen-I antibody titers were analyzed as described (Andreu et al., 2010). Briefly, ELISA plates were coated with collagen-I (1.0 μ g/well; Sigma-Aldrich) and diluted in sodium carbonate buffer (pH 9.3). Following overnight incubation at 4°C, plates were washed and then blocked using 1.0 % BSA for 1.0 hr. Serial 10-fold successive dilutions of serum were prepared in PBS-Tween/1.0 % BSA and added at room temperature for 2.0 hr. Plates were then incubated with biotinylated goat anti-mouse IgG for 1 hr, followed by streptavidin-HRP

(Amersham Biosciences, Buckinghamshire, England) for 30 min and developed with Sigma FAST OPD kit (Sigma) for 10 min. Enzymatic activity was stopped using sulfuric acid (3M). Optical density (OD) was measured at 450 nm with wavelength correction set to 540 nm on a SpectraMax 340 spectrophotometer (Molecular Devices, Sunnyvale, CA). Antibody concentrations were calculated using SoftMax Pro 4.1 (Molecular Devices). To determine Ig levels, serum ELISA was performed as described by the manufacturer's recommendations using the clonotyping system-HRP kit (SouthernBiotech).

Miles assay

Vascular leakage was measured as described (Sounni et al., 2010). Briefly, Evans blue dye (Sigma) was intravenously injected into anesthetized mice at 5.0 μ l/g, followed by cardiac perfusion with 1.0% paraformaldehyde in 0.05 M citrate buffer (pH 3.5) for 2 min at a flow rate of 5 ml/min. Tumors were collected and Evans blue dye extracted in 1.0 ml of formamide at 60°C for 24 hr, followed by quantitative detection at 610 nm using a SpectraMax 340 (Molecular Devices) using a standard curve to determine concentration. Total Evans blue extracted from tissue was then normalized to tissue weight.